Inversion of Meteor Rayleigh Waves on Earth and Modeling of Air Coupled Rayleigh Waves on Mars

Foivos Karakostas, Virgile Rakoto, Philippe Lognonne, Carene Larmat, Ingrid Daubar, Katarina Miljković

LA-UR-18-25160 (Accepted Manuscript)

Inversion of Meteor Rayleigh Waves on Earth and Modeling of Air Coupled Rayleigh Waves on Mars

Karakostas, Foivos
Rakoto, Virgile
Lognonné, Philippe
Larmat, Carene
Daubar, Ingrid

To be published in: Space Science Reviews

DOI to publisher's version: 10.1007/s11214-018-0566-6

Permalink to record: http://permalink.lanl.gov/object/view?what=info:lanl-repo/lareport/LA-UR-18-25160

Noname manuscript No.
(will be inserted by the editor)

Inversion of meteor Rayleigh waves on Earth and modeling of air coupled Rayleigh waves on Mars.

Foivos Karakostas · Virgile Rakoto · Philippe Lognonné · Carene Larmat · Ingrid Daubar · Katarina Miljković

Received: date / Accepted: date

Abstract Meteor impacts and/or meteor events generate body and surface seismic waves on the surface of a planet. When meteoroids burst in the atmosphere, they generate shock waves that subsequently convert into acoustic waves in the atmosphere and seismic waves in the ground. This effect can be modeled as the amplitude of Rayleigh and other Spheroidal modes excitation, due to atmospheric/ground coupling effects.

First, an inversion of the seismic source of Chelyabinsk superbolide is performed. We develop an approach in order to model a line source in the atmosphere, corre-

F. Karakostas
Institut de Physique du Globe de Paris, Planetology and Space Sciences
University Paris Diderot - Université Sorbonne Paris Cité
35, rue Hélène Brion, Case 7071, Lamarck A
Tel.: +33 1 57 27 53 18
Fax: +33 1 57 27 84 39
E-mail: karakostas@ipgp.fr

V. Rakoto
Institut de Physique du Globe de Paris, Planetology and Space Sciences
University Paris Diderot - Université Sorbonne Paris Cité , Paris, France

P. Lognonné
Institut de Physique du Globe de Paris, Planetology and Space Sciences
University Paris Diderot - Université Sorbonne Paris Cité , Paris, France

C. Larmat
Los Alamos National Laboratory, Solid Earth geophysics, Los Alamos, New Mexico, USA

I. Daubar
Jet Propulsion Laboratory, California Institute of Technology, Pasadena, California, USA

K. Miljković
Curtin University, School of Earth and Planetary Science, Perth, WA, Australia

sponding to the consecutive generation of shock waves by the interaction with the atmosphere. The model is based on the known trajectory. We calculate the synthetic seismograms of Rayleigh waves associated with the event by the summation of normal modes of a model of the solid part and the atmosphere of the planet. Through an inversion technique based on singular value decomposition, we perform a full Rayleigh wave inversion and we provide solutions for the moment magnitude.

SEIS will likely detect seismic waves generated by impacts and the later might be further located by remote sensing differential processing. In the case of Mars, we use the same method to obtain waveforms associated with impacts on the planetary surface or in low altitudes in the Martian atmosphere. We show that the contribution of the fundamental spheroidal solid mode is dominating the waveforms, compared to that of the first two overtones. We perform an amplitude comparison and we show that small impactors (diameter of 0.5 to 2 m), can be detected by the SEIS VBB seismometer of InSight mission, even in short epicentral distances, in the higher frequencies of the Rayleigh waves. We perform an analysis based on impact rate estimations and we calculate the number of detectable events of 1 meter diameter meteor impacts to be 6.7 to 13.4 per 1 Martian year for a $Q = 500$.

Keywords seismology · atmosphere · Mars · Rayleigh waves · meteor impacts · normal modes · airbursts.

1 Inversion of the seismic source for the Chelyabinsk airburst

1.1 Introduction

On February 15, 2013, a meteor entered the atmosphere of the Earth, approximately above the Russian city of Chelyabinsk. The time of its entry was about 09:20:00 local time (03:20:00 UTC) (Borovička et al., 2013). The phenomenon was well observed by the local population, as the celestial body created a tail of light and a sonic boom (Shuvalov et al., 2017). The entry was characterized by an important damage on the infrastructure, evidence of the presence of strong shock waves. The trajectory was recorded by numerous cameras on the ground and this kind of amateur data was provided on the worldwide web (see Zuluaga et al. (2013)).

It was also the largest seismic event associated to a meteoroid entry, ever recorded, only after the Tunguska event, which happened near the homonymous city of Siberia in 1908 (Ben-Menahem, 1975). The Tunguska event was recorded by at least four seismic stations (Ben-Menahem, 1975), whereas Chelyabinsk event occurred in an era when our home planet is well covered by a worldwide seismological network. Therefore, the available data for a thorough investigation of the generation and propagation of the seismic waves, associated to the event, raised the interest for further analysis of the characteristics of such a seismic source.

The orbit, trajectory and ablation process of the asteroid of Chelyabinsk was determined by Borovička et al. (2013). Brown et al. (2013) estimated the total amount of energy released by the meteoroid entry into the atmosphere. In the present work, the trajectory provided of Borovička et al. (2013) is used in order to model the con-

tinuous source in the atmosphere and the estimations of Brown et al. (2013) should be validated by the results of the inversion of the seismic source.

In addition to video recordings of the blast created by the meteoroid (Zuluaga et al., 2013), other kind of datasets provided evidence for the characteristics of the shock wave generated during the event. More precisely, de Groot-Hedlin and Hedlin (2014), performed an infrasound detection of the meteoroid using the USArray data in distances from 4000 to 6000 km and analyzed the properties of infrasonic waves associated to the event. Previously, Le Pichon et al. (2013) detected the event using data provided by the CTBTO infrasound sensors at distances up to approximately 8500 km.

Tauzin et al. (2013) performed an inversion of a purely seismic source. Their source point can be interpreted as the point on the solid surface mostly affected by the sonic boom. Heimann et al. (2013), inverted a source by full waveform fitting, assuming the source time function for an atmospheric explosion and finding out the best fitting epicenter for this source. In the present work, we seek to invert seismic record to retrieve the moving source generated by the shock waves of Chelyabinsk. The source is modeled as a continuously moving explosion in the atmosphere. The inversion is made without any assumption of duration of the seismic source but constrained from a model of released energy along the meteoroid trajectory based on physical parameter of the atmosphere that day.

1.2 The physical approach

We consider the meteoroid as a continuous seismic source into the atmosphere, following a known trajectory. In previous works, investigating the same event, an immobile source was used for the modeling, either situated on the ground (Tauzin et al., 2013) or in the atmosphere (Heimann et al., 2013). In those works, the duration of this point source was assumed in order to provide the moment magnitude of the event. In this work, we use the approach of a continuous source, consisted by consecutive explosions, in different altitudes and therefore different atmospheric conditions, whereas no assumptions are made for the duration of the source.

The meteoroid entry into the Earth's atmosphere generates a shock wave which is the result of the overpressure due to the force exerted by the meteoroid onto the ambient atmosphere (Edwards, 2009). The generated pressure, which characterizes the shock wave and its value depend on the meteoroid speed but also on the ambient atmospheric pressure and the time and distance traveled by the wave. Formulas describing the propagation of shock waves are developed in works focusing on the infrasound generated by airbursts (see a review in Edwards (2009)).

In this work, we examine the seismic Rayleigh waves recorded at distances far from the atmospheric near field, in stations situated on the ground. These waves are the result of the coupling effect between the atmosphere and the solid part of the planet of the generated shock waves. The generation and propagation of waves generated by a meteoroid and the coupling between the atmosphere and solid earth are shown schematically in Figure 1. In this figure, m_0, m_1 and m_2 correspond to the position of the meteoroid in $t = 0$, $t = 1$ and $t = 2$, respectively. When the meteor enters

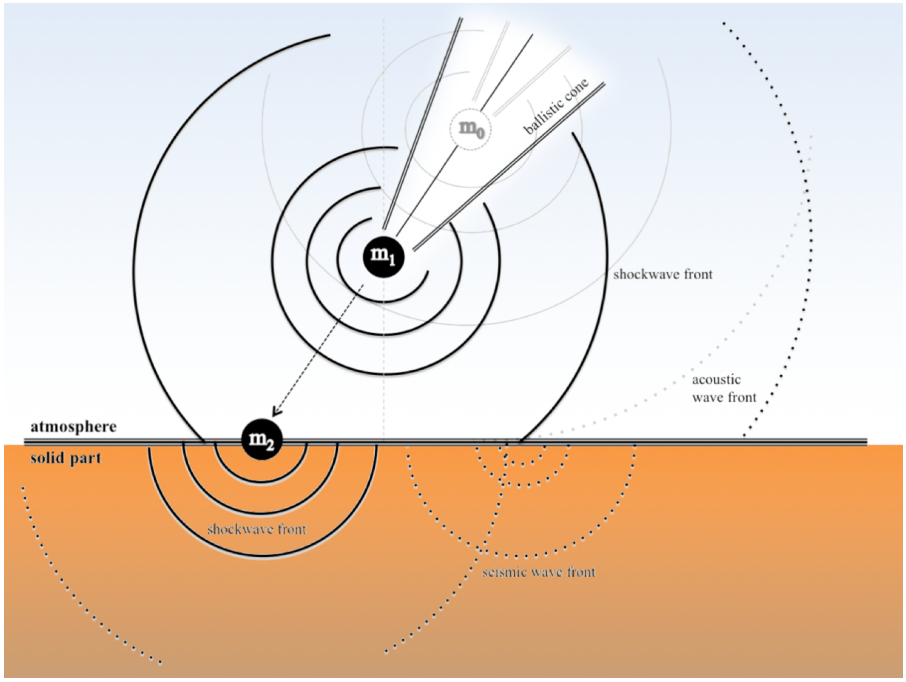

Fig. 1 Schematic model of a spherical meteoroid entering the atmosphere. The meteoroid is following a trajectory in the atmosphere before hitting the ground. The indices $0, 1, 2$ correspond to the position of the meteoroid in time, $t = 0$, $t = 1$ and $t = 2$ respectively. Shock waves, characterized by a nonlinear propagation regime are shown in continuous lines, whereas linear acoustic or seismic waves are represented by dashed lines.

the atmosphere it travels with a supersonic velocity. As happens with supersonic jets, the travel of the object at such high speeds creates a ballistic cone of an angle β, which is related to its speed. Shock waves are generated by this continuous source and then they propagate in a highly nonlinear regime before being converted to linear acoustic waves in the atmosphere, after a certain distance of propagation. In Figure 1, shock, nonlinear wavefronts, are represented with continuous lines, whereas the linear ones are shown by dashed lines. In the case of an impact or near ground explosion, the shock waves are propagated into the solid part, before being converted into linear seismic waves. The shock and acoustic waves generated in the atmosphere, are the source of surface waves, generated by the coupling effects between the atmosphere and the solid part.

Seismic data from stations located at long distances (hundreds of kilometers) from the event, cannot provide recordings corresponding to the nonlinear propagation of the generated waves in the atmosphere or the solid part. However, the seismic data are the result of all the seismic waves, generated by sources situated along and during the meteoroid travel in the atmosphere. Therefore, an inversion of the waveforms which are the result of these effects, should take into account the strength of the explosion in the whole entry process.

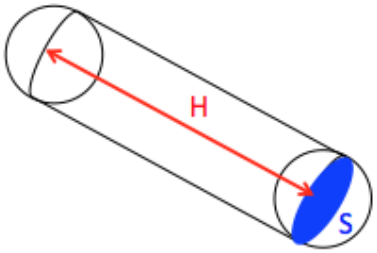

Fig. 2 The cylinder along the meteoroid trajectory represents the volume onto which the dynamic pressure of the projectile is applied. S represents the cross section of the meteoroid, whereas H indicates the remaining distance to the ground.

We design a model to do this. We consider the continuous explosion as the summation of several point explosions along the trajectory. Initially, we consider every explosion as isotropic, therefore, the wavefront of the shock waves shown in Figure 1 can be described as spherical. Every explosion is characterized by a moment tensor whose diagonal components are equal, $M_{11} = M_{22} = M_{33}$ and the moment tensor value is given by:

$$M_{ij} = -M_0 \cdot \delta_{ij} \tag{1}$$

Where M_0 is the seismic moment and δ_{ij} Kronecker's delta, equal to 1 for $i = j$ and to 0 if $i \neq j$.

For a meteoroid of a given size and a constant speed into the atmosphere, the moment tensor corresponds to the seismic energy released and it should not be considered constant along the trajectory. The released energy in a given point is given by the expression:

$$E = p \cdot V \tag{2}$$

where E stands for the Energy, p the pressure applied to the ambient atmosphere of volume V. The volume is characterized by a cylinder $V = S_{meteor} \cdot H$, whose base, S_{meteor}, is the cross-section of the meteoroid and its height H the remaining distance to the ground along its trajectory, as shown in Figure 2.

Pressure is proportional to the dynamic pressure of the entry of the meteor which is given by the expression:

$$q = \frac{1}{2}\rho_{atm} \cdot \upsilon^2_{meteor} \tag{3}$$

It must be noted here that in equation 3, with such high velocities the effects of gravity may be neglected.

Therefore, from the expressions 2 and 3, as the pressure, p, is proportional to the dynamic pressure q we can deduce that the same applies to the energy, E, which also depends to the volume V. Therefore, we can deduce the relative rate of the released energy from q.

Table 1 The trajectory of Chelyabinsk superbolide using explosions every 0.5 sec, based on the interpolation of the trajectory provided by Borovička et al. (2013). Indicated time is in seconds after 03:20:00 UTC, February 15, 2013.

Latitude (°)	Longitude (°)	Altitude (km)	Time*
54.4519	64.4963	95.46	21.00
54.4693	64.3612	92.45	21.50
54.4871	64.2265	89.48	22.00
54.5049	64.0918	86.51	22.50
54.5227	63.9572	83.55	23.00
54.5405	63.8226	80.59	23.50
54.5583	63.6879	77.62	24.00
54.5760	63.5533	74.66	24.50
54.5939	63.4186	71.69	25.00
54.6116	63.2839	68.72	25.50
54.6295	63.1492	65.75	26.00
54.6473	63.0145	62.78	26.50
54.6650	62.8798	59.83	27.00
54.6816	62.7429	56.97	27.50
54.6982	62.6062	54.10	28.00
54.7148	62.4694	51.24	28.50
54.7315	62.3325	48.37	29.00
54.7481	62.1957	45.50	29.50
54.7647	62.0589	42.64	30.00
54.7813	61.9219	39.77	30.50
54.7973	61.7840	36.97	31.00
54.8133	61.6461	34.16	31.50
54.8293	61.5082	31.35	32.00
54.8444	61.3731	28.62	32.50
54.8588	61.2407	25.96	33.00
54.8730	61.1131	23.40	33.50
54.8870	60.9880	20.90	34.00
54.8968	60.8979	19.10	34.50

Seismic moment is a portion of the total amount of released energy of the explosion. According to Lognonné et al. (1994) it can be expressed for an atmospheric source as:

$$M_0 = (\gamma - 1) \cdot E \tag{4}$$

where γ is the adiabatic index of an ideal gas, equal to $1 + \frac{2}{f}$ with f to be the degrees of freedom of a molecule of an ideal gas. Earth's atmosphere, composed mainly by diatomic nitrogen and oxygen, is considered as a diatomic gas and thus the degrees of freedom are $f = 5$ and therefore $\gamma = 1.4$. Therefore, the proportion of the seismic moment to the total amount of released energy for a meteoroid in Earth's atmosphere should be considered as:

$$M_0 = 0.4 \cdot E \tag{5}$$

With the application of the trajectory presented in Table 1, the obtained results for the moment are shown in Figure 3. In the top-left part, the density of the atmosphere above the region of Chelyabinsk is shown.

In the top-right, we represent the meteoroid speed calculated from the trajectory presented in Table 1. The instant velocity given at any time (t_i) is calculated as:

$$\upsilon(t_i) = \frac{\frac{x(t_i)-x(t_{i-1})}{t_i-(t_{i-1})} + \frac{x(t_{i+1})-x(t_i)}{t_{i+1}-(t_i)}}{2} \tag{6}$$

The position x is calculated in 3D Cartesian coordinates, given the altitude, latitude and longitude of the meteoroid.

In the bottom-left, the time evolution of the meteoroid altitude is presented. The effect at the last second, with the decrease of the altitude appearing to have a lower rate, is linked to the deceleration observed in the Figure of meteoroid speed.

It is observed that there is a sharp deceleration after 03:20:33.5 UTC (in our resolution of 0.5 seconds). This effect has a direct impact on the moment, which is presented in the bottom-right part. The largest absolute value of the moment is considered equal to 1 at 03:20:33.5 UTC and all the other values are represented as fractions of it. It is clearly observed that the main part of the energy is released during the last 3 seconds of meteoroid's motion in the atmosphere. More precisely, only the explosions after 03:20:30 UTC should relase more than 5% of the energy released at the peak point. However, as demonstrated later, the amplitude of the normal modes for sources at higher altitude is greater too. This means that the contribution of a point source in high altitude to the calculated seismogram is greater than the relative value of its moment tensor compared to those of the point sources in lower parts of the atmosphere.

1.3 A linear approach for a nonlinear source

We seek to model the bolide as a succession of seismic sources that can be linearly summed. However, shock waves are not linear, so we need to define our individual source in a way to avoid to include a shock waves description. In the following we show that this corresponds to some temporal limitations. According to Edwards (2009) the radius of the blast generated by the meteoroid can be calculated by the following equation:

$$R_0 = M \cdot d_m = \frac{\upsilon_{meteor}}{C_s} d_m \tag{7}$$

where d_m is the diameter of the meteoroid, which is estimated at about 20 meters for Chelyabinsk and M is the quantity corresponding to $\frac{1}{sin\beta}$, where β is the angle of the Mach cone, given by the expression:

$$sin\beta = \frac{C_s}{\upsilon_{meteor}} \tag{8}$$

Applying an average sound speed of $300\, m.s^{-1}$, an average $\upsilon_{meteor} = 18.33\, km.s^{-1}$, derived by the known trajectory (Borovička et al., 2013) and presented in the top-right part of Figure 3, and the meteoroid diameter in our calculations we find an $R_0 = 1255\ m$. In the work of Edwards (2009), which is a review of previous works on shock waves generated by meteoroids, it is noted that the shock wave is converted

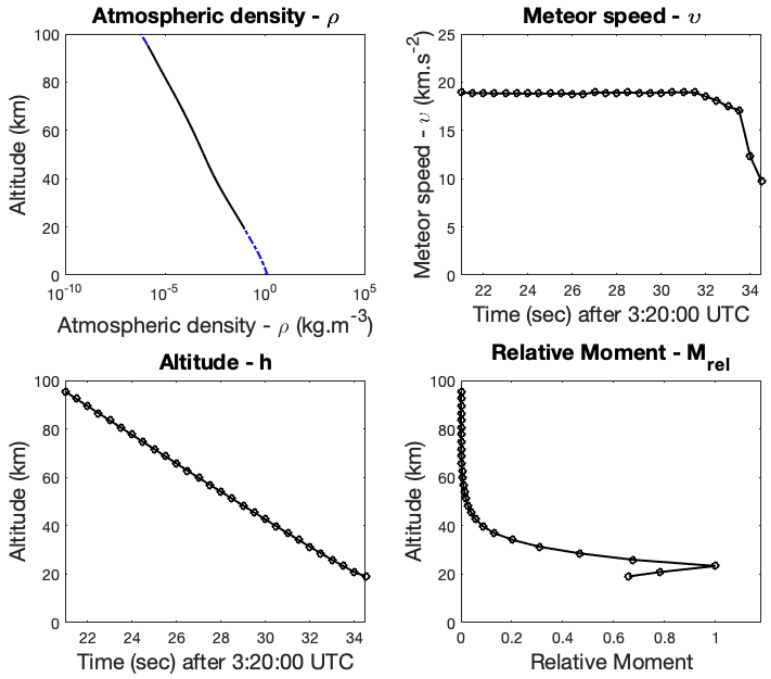

Fig. 3 The atmospheric density in Chelyabinsk, the meteoroid speed, its altitude and the relative moment are shown in the top-left, top-right, bottom-left and bottom-right figures respectively. The atmospheric density is obtained by the *NRLMSISE-00* model, used for the calculation of synthetic seismograms, whereas its altitude is provided by the interpolation of the trajectory calculated by Borovička et al. (2013). Meteoroid speed is calculated by differentiation of the trajectory (see details in text). The results presented here are used to constrain the evolution of the seismic moment during the bolide entry used in the seismic inversion.

into a weakly nonlinear wave after several R_0 distances. According to ReVelle (1974), this weakly nonlinear regime exists for a variable amount of time.

In order to choose the temporal resolution for our study, we had to obey to this rule and model explosions that will happen in distances more than several R_0 apart. Therefore, we calculated the time needed by the meteoroid, in order to traverse this distance. This time should be 0.066 seconds and therefore we should multiply this several times in order to obtain a satisfactory condition for our temporal resolution. In 0.5 seconds, the meteoroid is already more than $7R_0$ far from the previous explosion and this is the reason that we used this temporal resolution to our analysis. We should note that in the final part of the continuous explosion, where the meteoroid speed is decreasing, R_0 decreases as well and the temporal resolution provides results for sources situated more R_0 distances apart.

1.4 Data selection

In order to investigate the source properties we perform an inversion of the Rayleigh waves generated by the event. The data were provided by the Global Seismographic Network (GSN). Each recording consists of a 2-hour data series of the day of the event (February 15, 2013), from 02:50:00 UTC to 04:50:00 UTC, which means from 30 minutes prior to 90 minutes after the event.

Raw data from 134 stations were examined with the objective to find the best quality of Rayleigh waveforms. This strategy was chosen because our aim was not only to characterize the seismic event, but use data which permit to thoroughly investigate the signature of an atmospheric continuous source. Therefore, any kind of waves of any other origin should be avoided, as well as the noise in a relatively large Rayleigh waves frequency band. The recordings were filtered for frequencies between 0.015 Hz and 0.050 Hz after correction of instrument's response.

The first step was the selection of data, which contain Rayleigh waves generated by Chelyabinsk meteoroid, at epicentral distances up to 40 degrees. For doing so, the 3 channels of the recordings, 2 horizontal (N and E) and one vertical (Z), were rotated horizontally, in order to obtain the radial (R) and transverse (T) component of the seismogram. This rotation helps to identify the Rayleigh waves generated by Chelyabinsk meteoroid, as they should be apparent only in the vertical and radial components of the seismograms and not in the transverse ones. We performed this rotation in displacement, velocity and acceleration waveforms, in order to increase the certainty of the selection, but also to investigate all of them with an inversion technique. In the meantime, we made sure to include in our selections, recordings from stations with azimuth all around the epicenter, in order to secure adequate azimuthal coverage, capable to reveal eventual directivity.

Data selection was done after tracing the seismograms in relative distances from an "epicenter", which was assumed, for the needs of this step only, as the projection on the ground of the position of meteoroid at 03:20:32 UTC, according to the trajectory provided by Borovička et al. (2013). The selection of this position was made after observing the evolution of the meteoroid speed in the atmosphere. It corresponds to the point where a rapid deceleration is starting.

It is important to note that the trajectory provided and shown in Table 1 is based on the observations made by Borovička et al. (2013) but it is interpolated in order to obtain the meteoroid position for every 0.5 seconds. Based on this interpolated trajectory, we calculated the meteoroid speed in every position. The time resolution could be even greater, but the reason for this time step serves the strategy of the source modeling discussed in detail in section 1.3.

The filtered data, for the selected stations, all located at epicentral distances up to 40° are shown in Figure 4. The amplitudes of the waves are all equally normalized for the three channels and for all the stations. It is shown that the transverse component recordings are much less important as it concerns the waveforms, which should correspond to Chelyabinsk meteoroid, whereas they are well observed in both radial and vertical component. The relative absence of any transverse signal in the travel-time curve associated to Chelyabinsk is a criterion to include the recordings of a station in our selection, as the chosen frequency band allows only the waveforms of Rayleigh

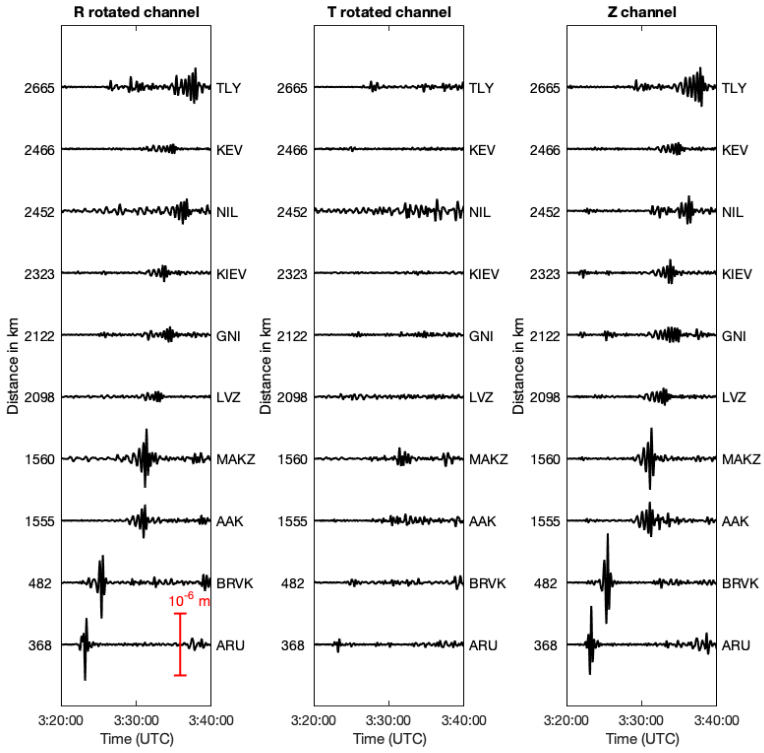

Fig. 4 The rotated and filtered (0.015 Hz - 0.050 Hz) data of the selected stations. The seismograms of the displacement are projected in an order of epicentral distance. The amplitudes are multiplied by a factor of $2 \cdot 10^9$.

waves to appear, which, if associated to Chelyabinsk event, should be characterized by the presence only of the radial component in these rotated seismograms.

The events of magnitude $M \geq 4$ until the end of these time series (i.e. 04:50:00 UTC), of February 15, 2013, according to the International Seismological Center (International Seismological Centre, 2013), are presented in Table 2. The catalog is dominated by events in the South Pacific Ocean, most precisely at Kermadec and Tonga trenches and the most important event prior to the Chelyabinsk superbolide, is the earthquake of $M = 5.8$ in Tonga (also highlighted in Table 2).

In a second step, the waveforms of Rayleigh waves generated by Tonga earthquake should be identified, in order to verify that the selection we have performed is done correctly, providing for further investigation only the signature of Chelyabinsk. This task is also performed and presented in previously (Tauzin et al., 2013). The procedure for the identification of the waveforms associated to Tonga earthquake was identical to this applied to Chelyabinsk and described in this section. In total,

Table 2 The seismic events of $M \geq 4.0$ from 00:00:00 to 04:50:00 UTC, February 15, 2013, according to the International Seismological Centre (2013). Positive values represent North and East latitude and longitude respectively, whereas negative correspond to South and West.

Time (UTC)	Latitude (°)	Longitude (°)	Depth (km)	M	Region
00:24:42.10	-11.4679	165.5266	24.0	4.0	Santa Cruz, Solomon Islands
00:53:39.37	-10.8049	164.9543	10.0	4.1	Santa Cruz, Solomon Islands
02:28:48.64	-22.8549	170.1281	25.0	4.2	New Caledonia
02:43:37.55	34.7022	73.0360	21.0	4.0	NE Pakistan
02:44:35.75	-23.7839	-177.2334	0.0	4.2	South Pacific Ocean
02:51:28.04	-19.7439	-179.3703	700.0	4.3	Fiji
03:02:22.76	**-19.8605**	**-174.3665**	**74.7**	**5.8**	**Tonga**
03:06:00.70	16.1060	-98.1620	2.8	4.0	Oaxaca, Mexico
03:21:20.80	-31.5930	-69.6590	112.7	4.0	San Juan Province, Argentina
03:22:08.30	**54.4841**	**62.2259**	**0.0**	**4.2**	**Chelyabinsk Oblast, Russia**
03:23:32.07	-10.7484	165.2987	31.0	4.3	Santa Cruz, Solomon Islands
03:46:21.00	-10.8425	165.7472	10.0	4.0	Santa Cruz, Solomon Islands
04:26:49.75	-30.3418	-177.4974	33.0	4.5	Kermadec, New Zealand

we selected 10 among 134 stations, with 30 of them located at epicentral distances smaller than 40°.

1.5 Calculations of synthetic seismograms with normal mode summation

We calculate synthetic seismograms with the method of normal modes summation (Lognonné et al., 1998) for every selected station as explained in section 1.4. The normal modes are computed for a 1D symmetrical model describing the solid Earth and the atmosphere. The solid part is the combination of *PREM* (Dziewonski and Anderson, 1981), a local lithospheric model for Chelyabinsk (Myers et al., 2010) and the empirical atmospheric model *NRLMSISE-00* (Picone et al., 2002). We consider a non rotating Earth with spherical symmetry.

The synthetic seismograms are the summation of the fundamental spheroidal mode branches, for angular moments $l = 1\ to\ 800$ which correspond to frequencies of $3 \cdot 10^{-4}$ Hz to 0.067 Hz. The contribution of the overtones is negligible as it concerns the surface waves (see more details in section 2.2).

Synthetics were calculated for the horizontal and vertical direction of every station (N, E, Z) and for every component of the moment tensor separately. The objective of this step was to investigate the contribution of every component on the waveforms of Rayleigh waves.

In Figure 5 the synthetic seismograms for every diagonal component of the moment tensor, are shown, calculated for AAK station, situated in Ala Archa, Kyrgyzstan, at a distance of 1555 km far from the "epicenter" of Chelyabinsk event. The moment tensor used for these calculations is $M_0 = 10^{14}\ N \cdot m$ (which, in the case of an isotropic source, it corresponds to a moment magnitude of $M_W = 4.1$) and it concerns a point source occurring at 03:20:33.5 UTC, which is the time of the maximum energy released in the modeling of the continuous source, as shown in Figure 3 and described in section 1.2. The synthetic seismograms used for the source inversion

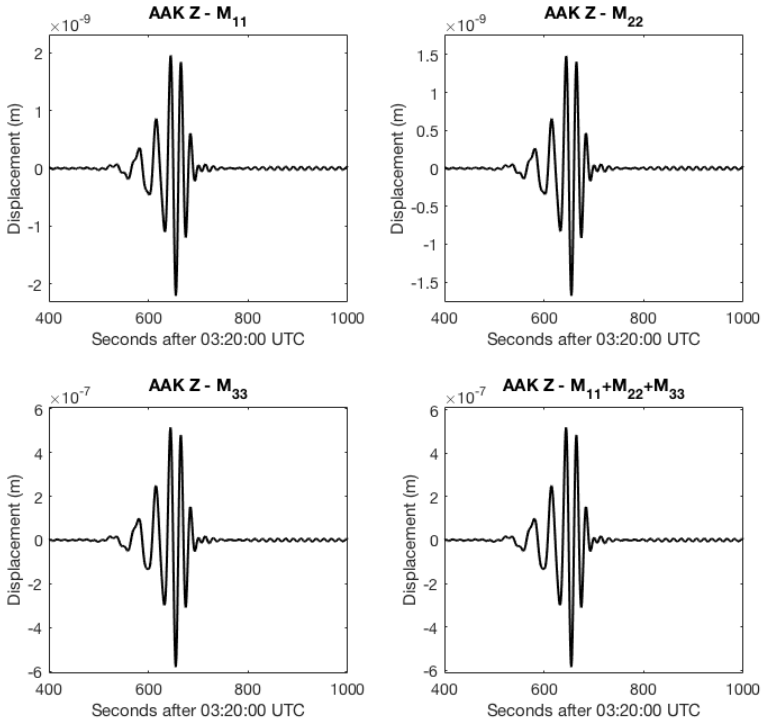

Fig. 5 The computed seismograms for the diagonal components M_{11}, M_{22}, M_{33} and an isotropic source where $M_{11} = M_{22} = M_{33}$ for station AAK situated 1555 km far from the final explosion of the modeled source for Chelyabinsk. The diagonal components M_{11} and M_{22} have a minor contribution to the amplitude, less than 1% of the amplitude of Rayleigh waves calculated for M_{33} component.

(shown in Figure 6), are the sum of every seismogram of every point source which constitutes the line source.

We found out that the diagonal components M_{11} and M_{22} have a minor contribution to the amplitude, less than 1% of the amplitude of Rayleigh waves calculated for M_{33} component. Given that we used an isotropic source, where $M_{11} = M_{22} = M_{33}$, knowing that the contribution of M_{33}-seismogram is dominating this result helps to understand that the inversion is taking into account mostly the waveform provided by this component and the other two may vary but in an inconsiderable scale. The top-left and top-right seismograms are the synthetics calculated for M_{11} and M_{22}, respectively. Their displacement peak amplitude is a bit less than $2 \cdot 10^{-9}$ m. In the mean time, the bottom-left seismograms correspond to the calculated synthetic seismogram for the M_{33} component and its peak amplitude is about $5 \cdot 10^{-7}$ m, whereas the same peak amplitude applies to the synthetic seismogram of displacement calculated for an isotropic source where $M_{11} = M_{22} = M_{33} = 10^{14}$ $N \cdot m$. Similar results are found for every one of the selected stations. Amplitudes depend linearly on the

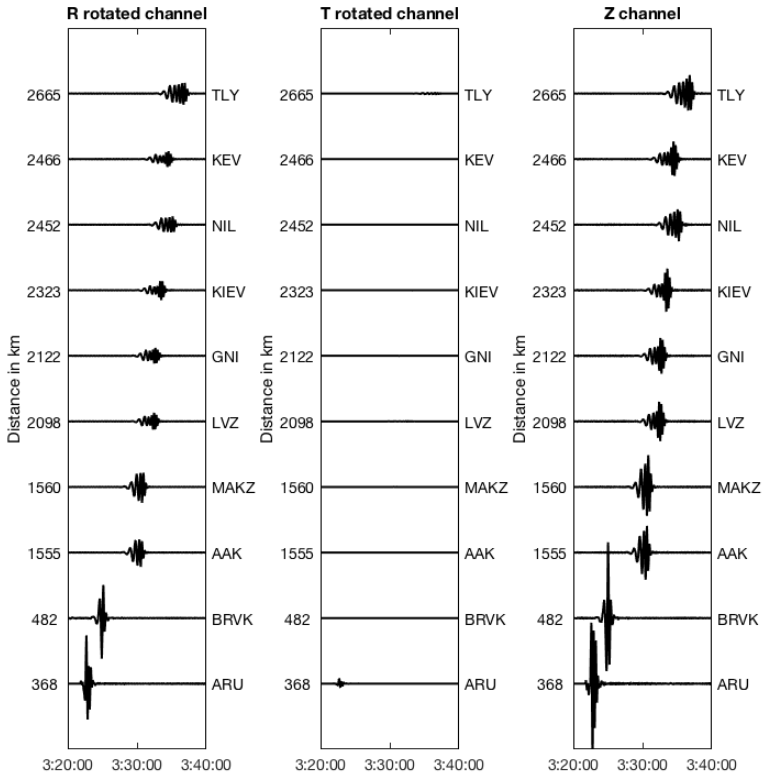

Fig. 6 The rotated synthetic seismograms, calculated for every one of the selected stations, for a line source of $M_0 = 4.49 \cdot 10^{14}\ N \cdot m$ ($M_W = 4.1$). In the graphs the two rotated horizontal (radial, R, and transverse, T) components and the vertical component (Z) are shown. Seismograms are filtered for a frequency band of 0.015 Hz to 0.050 Hz. The amplitudes are multiplied by a factor of $2 \cdot 10^9$ for every station.

value of M_0 and we will therefore determine this value by a linear inversion, which is described in section 1.6.

In a second step the seismograms were rotated in order to obtain the radial (R) and transverse (T) component in a procedure equal to this performed for the data. The horizontal (E and N), rotated (R and T) and vertical (Z) component, for point sources occurring every 0.5 seconds, from 03:20:21.0 UTC to 03:20:34.5 UTC, were then summed in order to obtain the seismogram corresponding to the line source for every station.

In Figure 6 the synthetic seismograms for the radial (R), transverse (T) and vertical (Z) component for every station, generated by a line source of moment $M_0 = 4.49 \cdot 10^{14}\ N \cdot m$ ($M_W = 4.1$) are shown. It is clearly seen that the Rayleigh waves are well modeled, as the associated waveforms don't appear in the transverse component. Seismograms are filtered for a band frequency of 0.015 Hz to 0.050 Hz. The

amplitudes are multiplied by a factor of $2 \cdot 10^9$, in an equal way as it is already done for the recordings in Figure 4. Therefore, as the amplitudes are greater in this modeling, compared to the data, there is a first evidence that the real source should be characterized by a smaller moment than the one used for this modeling.

1.6 Inversion of the seismic source

As discussed in previous section 1.5, the diagonal components of the moment tensor for $i = 1,2$ obtain much smaller amplitudes, with a contribution less than 1% to the synthetic seismogram obtained for the diagonal component M_{33}. Therefore, a full waveform inversion for a non-isotropic source, even if it can provide an almost perfect fit between data and synthetics, should be avoided, as there is little sensitivity to the non-radial components of the moment tensor. Therefore, we chose to only invert the radial component of the moment tensor, as performed in other studies (Heimann et al., 2013) for a single point source.

We perform the inversion in the horizontal (E, N) and vertical (Z) components of the seismogram, in order to obtain the best fit to the synthetic seismograms presented in section 1.5 with the recordings. This procedure is done for filtered seismograms between 0.015 Hz and 0.050 Hz.

The inversion of the full waveform for the Rayleigh waves is based on the singular value decomposition method (Rakoto et al., 2018) and its concept is given by the equation 9, which gives the value of the moment tensor for the best fit between the data used and the synthetic seismograms:

$$\frac{\partial}{\partial M_{ratio}}[\int_{t_1}^{t_2}(s_{synt}(t) - s_{obs}(t))^2 dt] = 0 \tag{9}$$

where M_{ratio} is the result of the inversion, expressed as a ratio of the M_{real} corresponding to the best fit of the recordings and the M_{synt} used for the synthetics input.

$$M_{ratio} = \frac{M_{real}}{M_{synt}} \Rightarrow M_{real} = M_{synt} \cdot M_{ratio} \tag{10}$$

t_1 and t_2 represent the initial and last time of the selected time series, corresponding to the Rayleigh waveform. s_{synt} is the part of the synthetic seismogram between t_1 and t_2 and s_{obs} the data for the same time period. This part of the time series is shown in red in Figure 7.

In order to perform the inversion for multiple stations, we build a unique artificial signal for both s_{obs} and s_{synt} by placing the Rayleigh waveforms one after the other.

1.7 Inversion results

In a first step we perform an inversion separately for every station and for every component (N, E, Z). Then, we apply the same inversion by increasing progressively the number of used stations, in order to observe the contribution of every waveform to the result of a unique source which provides the seismograms with the best fit with

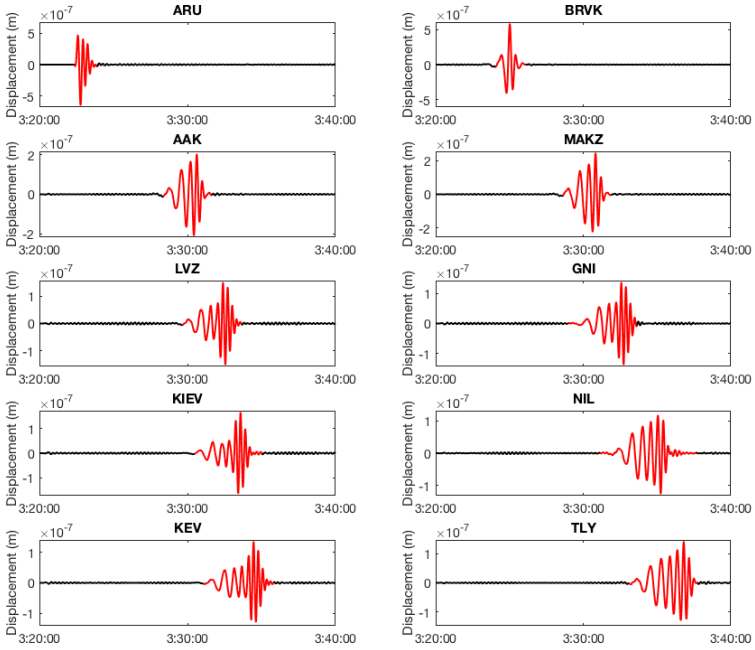

Fig. 7 The synthetic seismograms for the displacement of the vertical (Z) component are shown in black, whereas red color represents the part of the seismograms used for the inversion.

the entire dataset. The first step can provide useful information about the geographical distribution of our results, whereas the second one shows the contribution of every station to the unique source for every component provided in the end.

1.7.1 Inversion of the source for every station separately

As referred in section 1.6, the inversion technique was applied to the displacement, velocity and acceleration seismograms of horizontal (N, E) and vertical (Z) components of every station separately.

The inversion was not performed in the whole time series of the seismograms, but it was limited to the Rayleigh waveform provided by the synthetic seismograms. In Figure 7, the synthetic seismograms of the vertical component of displacement are shown in black, whereas red color represents their part used for the inversion. It is important to note that this selection in the vertical component, which provides larger amplitudes than the horizontal ones, contributed to identifying the Rayleigh waveforms in the horizontal components characterized by a smaller signal to noise ratio.

In Figure 8 the results obtained for the displacement at AAK station are shown. The recordings are shown in black, whereas the red line corresponds to the syn-

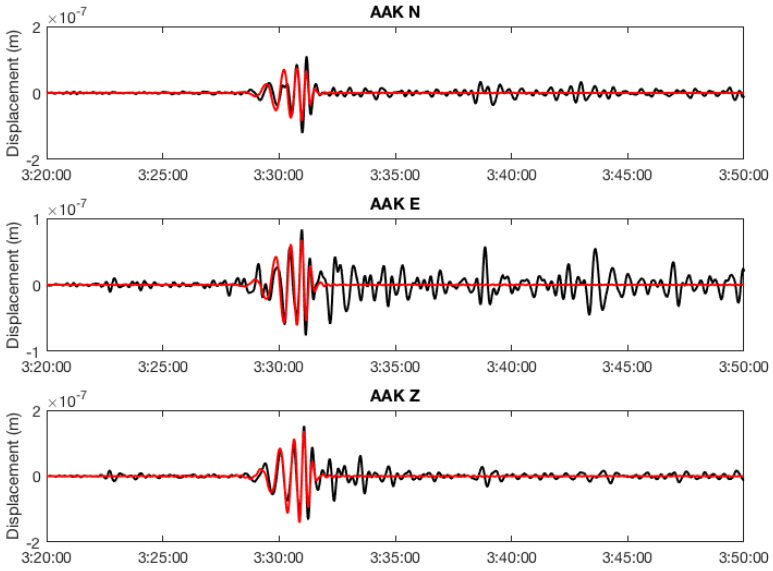

Fig. 8 The synthetic seismograms calculated after the performed inversion for the displacement seismogram of AAK station, in horizontal (E and N) and vertical (Z) components. The data are shown in black and the synthetic seismograms in red. Both data and synthetics are filtered in a frequency band from 0.015 Hz to 0.050 Hz.

thetic seismogram, after the inversion, equivalent to $s_{synt} \cdot M_{ratio}$ (see section 1.6). The best fit for N horizontal component suggests a seismic magnitude of 3.54, using the Hanks-Kanamori magnitude scale (Hanks and Kanamori, 1979), whereas the E component has the best fit for a magnitude of 3.53 and the Z, vertical one, for 3.46.

The results of the magnitude that satisfies the vertical component of the acceleration seismogram, for every station, are shown on a map in Figure 9. The trajectory of the meteoroid is shown in red color and it has a direction from ESE towards the WNW. The magnitudes for the best fit of the acceleration vertical component are situated in the location of every station.

All the results for the moment magnitude obtained by the separate inversion of the seismograms of every component of every one of the selected stations are shown in Table 3. We observe that the same geographical trend found for the vertical component of the acceleration holds for every component of displacement, velocity or acceleration. The moment magnitude provided by the inversion technique is greater for the horizontal components. This effect is associated with the smaller signal to noise ratio compared with the one corresponding to the vertical component. Therefore, the results of the vertical component can be considered of better quality. Nevertheless, the ability to model the horizontal components, with provided sources which do not differ largely from the horizontal ones in terms of Rayleigh waves amplitudes,

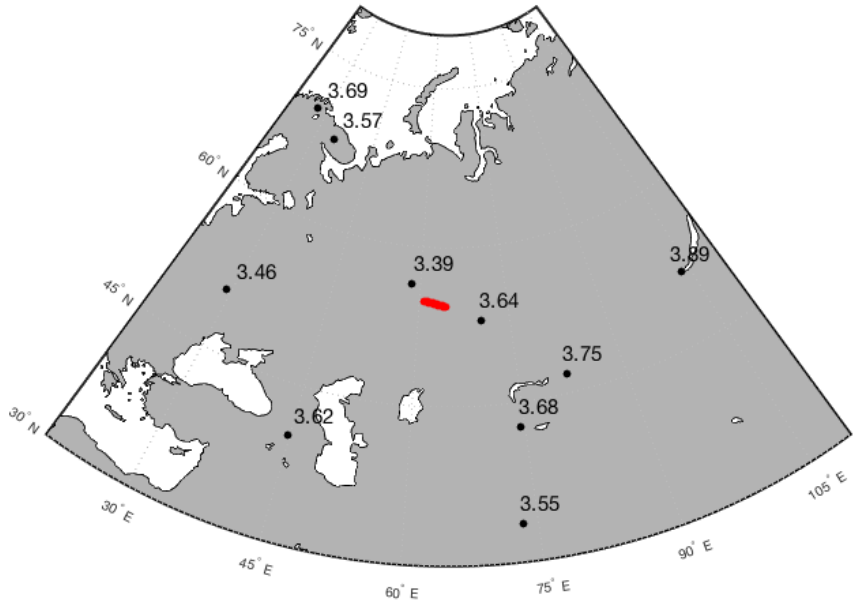

Fig. 9 The magnitude for every source providing the best fit between the acceleration vertical seismogram of every station and the respective synthetic seismogram calculated by normal modes summation.

Table 3 Moment magnitude provided by the inversion of Rayleigh waves for every component of every station.

	Displacement			Velocity			Acceleration		
Station	N	E	Z	N	E	Z	N	E	Z
ARU	3.54	3.53	3.46	3.38	3.42	3.26	3.52	3.54	3.39
BRVK	3.56	3.66	3.59	3.42	3.52	3.42	3.65	3.75	3.64
AAK	3.70	3.78	3.62	3.59	3.62	3.45	3.82	3.88	3.68
MAKZ	3.80	3.88	3.73	3.63	3.74	3.55	3.87	4.01	3.75
LVZ	3.64	3.72	3.63	3.35	3.48	3.38	3.55	3.69	3.57
GNI	3.53	3.67	3.56	3.54	3.69	3.44	3.78	3.89	3.62
KIEV	3.37	3.51	3.40	3.35	3.38	3.23	3.59	3.64	3.46
NIL	3.71	3.95	3.61	3.61	3.89	3.49	3.82	4.12	3.69
KEV	3.65	3.69	3.58	3.32	3.44	3.33	3.63	3.68	3.55
TLY	3.78	3.66	3.66	3.72	3.63	3.59	4.03	3.93	3.89

is an element showing that the modeling and inversion technique are able to provide adequate results even for recordings with smaller signal to noise ratio.

It is observed that the obtained values for the moment magnitude appear to be slightly greater in the west side of the source, compared to those obtained for the stations located at the east. This observation is shown also in Figure 10, where the provided magnitudes for the stations located at the west side of the source are shown

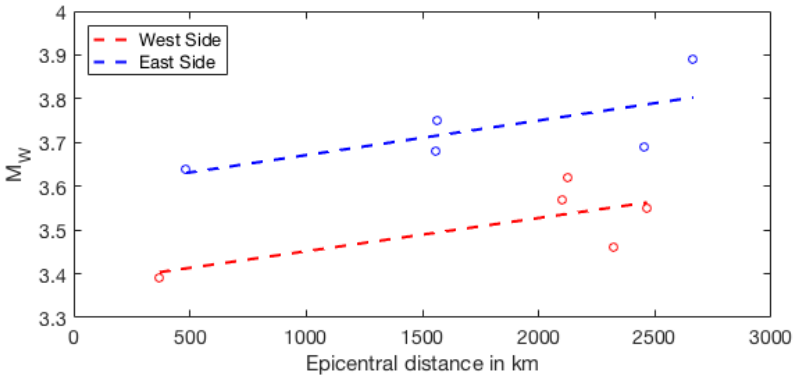

Fig. 10 The magnitudes provided by the inversion technique for the set of selected stations is shown for the vertical component of acceleration seismogram. The red dots indicate magnitudes for the stations situated at the west side of the source, whereas the blue dots indicate the respective magnitudes for stations at the east side. Dashed lines are adjusted polynomials of 2nd degree to the results. We notice that the provided magnitudes for stations at the east side are greater than those for the west side. This effect is an evidence of a Doppler effect associated with the directivity of the source (see details in text). The increase rate of the magnitudes with distance corresponds to a minor dispersion apparent on the recordings.

in red and those of the east side in blue color. Taking into account that the source is moving from ESE to WNW, this effects could be associated to the directivity of the source and a Doppler effect.

Stations located on the west side of the source, are approached by the moving source and therefore their recordings should be characterized by relatively smaller amplitudes, as the attenuation is most important for higher frequency waves. Therefore, the synthetic seismograms, which don't take into account the Doppler effect, should provide larger amplitudes compared to the data on the west side and the inversion results provide smaller magnitudes.

In the mean time, as the stations at the east side "see" the source traveling away from them, they should record data characterized by smaller frequencies and therefore smaller attenuation. Consequently, the recordings on the east side should be of greater amplitude (compared to the west side), whereas the calculated synthetics, should be smaller compared to the recorded data. Therefore, the inversion for these stations should provide greater magnitudes.

In order to verify the presence of such an effect we calculate the spectra of the vertical component of displacement, as shown in Figure 11. The spectra for the stations located at the west side of the source are shown in red, whereas those for the stations at the east side in blue. Given that the meteoroid is moving mostly towards the West, the west side seismograms should be identified by higher frequencies. This effect is clearly seen in the curve corresponding to the closest station, ARU, which is the red curve of higher amplitude density and has a peak at frequencies greater than 0.4 Hz. The rest set of red curves is characterized by a smaller amplitude density, compared to the blue curves, corresponding to the stations at the East. The dotted lines represent the mean value of the maximum amplitude density for the stations at the West and East, in red and blue respectively. It is shown that this is slightly greater for the

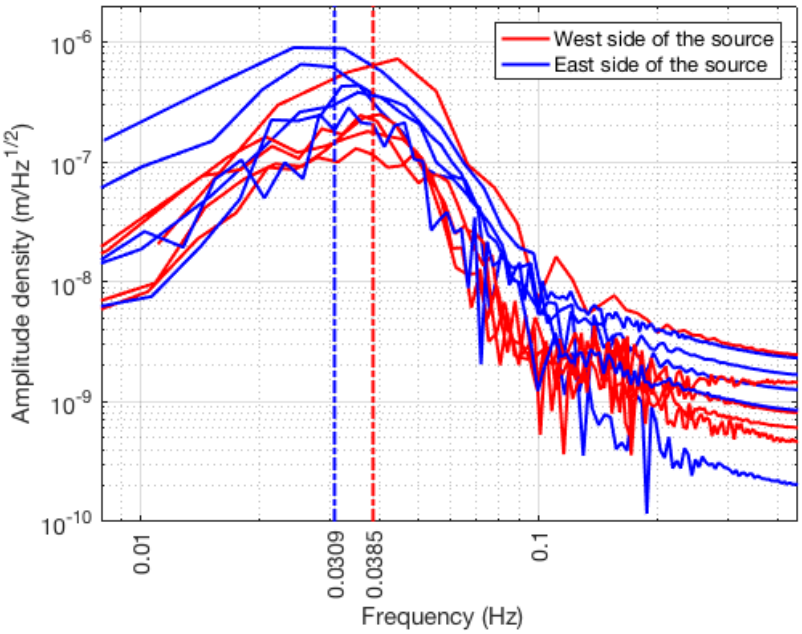

Fig. 11 The spectra for the stations located at the west side of the source are shown in red, whereas those for the stations at the east side in blue. A smaller amplitude density characterizes the set of red curves, compared to the blue ones. The dotted lines represent the mean value of the maximum amplitude density for the stations at the West and East, in red and blue respectively. It is shown that this is slightly greater for the stations at the west side and it corresponds to a clear presence of a Doppler effect associated to the directivity of the source.

stations at the west side and it can be an evidence of the presence of the described Doppler effect associated to the directivity of the source.

The slight difference of the amplitude density between the data of the stations at the east and west side of the source cannot describe alone the difference at the inversion results. Therefore, the presence of this directivity at the synthetics should explain them. In order to find out if this hypothesis is true, we calculated synthetic seismograms for seismic stations located at equal epicentral distances (10°) on the east and the west side of the source, in azimuths from 80° to 100° and 260° to 280° respectively.

The amplitude density of these seismograms is shown in Figure 12. Seismograms for stations located at the East are shown in blue, whereas those for stations located at the West are shown in red color. It is observed that the stations that “see” the source moving away (those located at the East) provide synthetics with a greater amplitude density in lower frequencies, compared to those that “see” the source approaching. Furthermore, the maximum amplitude density is observed at the higher frequencies (between 0.06 and 0.07 Hz) of the synthetics calculated for stations at the west side of the source. These observations firstly validate more clearly the Doppler effect, which is slightly observed in the case of data, which are characterized by a distribution of

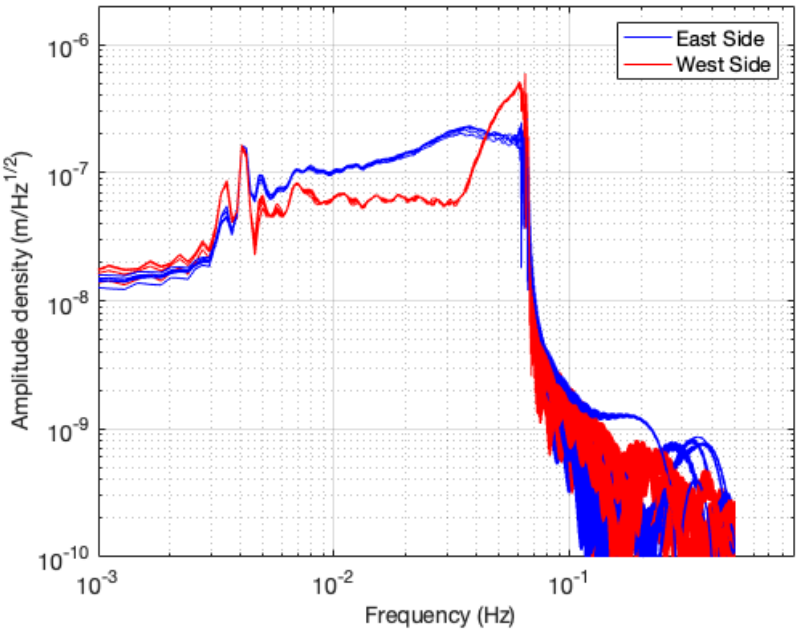

Fig. 12 The amplitude density of synthetic seismograms for stations at an epicentral distance of 10° at the East (blue) and West (red) side of the source. It is observed that synthetics at the East are characterized by higher amplitude density in lower frequencies, whereas the maximum amplitude density is obtained for the higher frequencies of the West side synthetics. This effect validates the slight difference observed in data and explains the moment magnitude difference, obtained by the inversion technique.

epicentral distances and therefore the effect cannot be so clear, as other factors (for example the local lithospheric structure) contribute to the recorded signal. Secondly, they explain the lower values for the seismic moment, provided by the inversion on the west side data, as the higher amplitude in synthetics satisfies a smaller seismic source, through the comparison with real data.

1.7.2 Inversion of a unique source by simultaneous inversion of seismograms from all stations

After the investigation of the inversion results, performed separately for every component of the seismograms of every station, we performed a simultaneous inversion, in order to provide a unique source, which satisfies the recordings of every station at once. This task was done progressively, in order to observe the contribution of every seismogram from each station to the obtained result. This means that starting from the source provided for the closest station to the source (ARU), we continued by obtaining the source that provides the best fit to the recordings of the couple of closest stations and so on, up to a source inversion for all the selected stations.

The applied technique was to provide data series that consist an ensemble of the seismograms from all the stations. In Figure 13, the vertical component of the

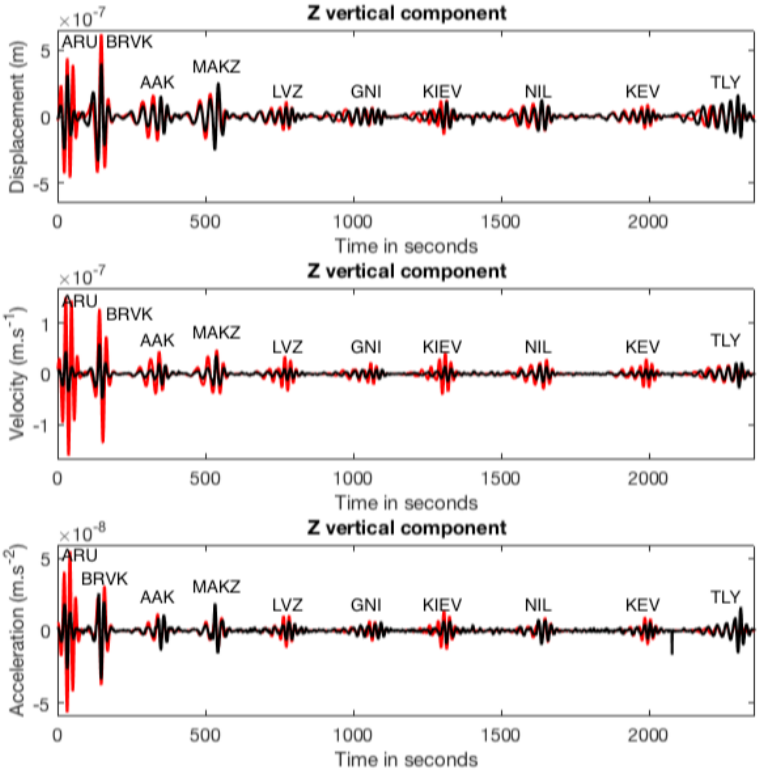

Fig. 13 The combined dataseries corresponding to the vertical component of the selected part of signal of the recordings and synthetic seismograms from every station, used for the inversion of a unique source.

displacement, velocity and acceleration seismograms of every station is shown. Black color represents the recordings, whereas red corresponds to the synthetics, s_{synt} of the equation 9, which represents the inversion technique. The station that provides every part of the data series is noted above the corresponding Rayleigh waveform.

The obtained results of this technique, provided the source in terms of magnitude moment presented in Table 4. It is observed that the magnitude obtained by the inversion of horizontal components is greater, for the reason that is discussed previously in 1.7.1, although, the results of every component don't appear to differ largely. In the vertical component, the obtained results for displacement and acceleration are in good agreement, whereas the velocity seismograms provide a smaller magnitude.

These results, for the vertical component of the displacement seismogram of the ensemble of the stations, are shown in Figure 14. We can observe that the unique source, provided by the inversion technique and corresponding to a moment tensor whose diagonal components are $M_0 = 1.25 \cdot 10^{14}$ to $4.04 \cdot 10^{14}$ N.m, provide re-

Table 4 Moment magnitude provided by the inversion of Rayleigh waves for every component and for a unique source providing the best fit to the recordings of the ensemble of the selected stations.

Seismogram	Displacement	Velocity	Acceleration
N	$M_W = 3.64$	$M_W = 3.47$	$M_W = 3.62$
E	$M_W = 3.68$	$M_W = 3.52$	$M_W = 3.70$
Z	$M_W = 3.57$	$M_W = 3.36$	$M_W = 3.52$

sults that agree well with the waveforms and the amplitudes of the Rayleigh waves, recorded by the instruments of the selected stations.

1.8 Synthetic seismograms calculation with spectral element method

In order to assess the potential role of effect of the 3D structure on the previous results, we performed the calculation of synthetic seismograms for an 1D spherical model and a model containing the lateral variations of crustal and upper mantle structure (3D model), with the use of a spectral element method software, *SPECFEM Globe* (Komatitsch and Tromp, 2002a,b). The simulations were performed for one chunk of Earth covering an area of 6000 km by 3500 km centered around 55° E and 57.5° N. The resolution of the modeling was 7.5 seconds with a number of elements of 640 along the NS side of the model, 384 along the WE side and 423 radially. The crust was represented using 4 elements. With this resolution, the maximum size of an element edge is 32km.

The model of internal structure for the unidimensional case is *PREM* (Dziewonski and Anderson, 1981), whereas in the case of the 3D model a combination of a model of internal structure, *s362iso* (Bassin et al., 2000) and higher resolution European model *EUCrust7.0* (Tesauro et al., 2008) was used, including topography, ocean, attenuation, gravity and rotation effects.

Seismograms are computed for a single point that is excited by a Heaviside function. The single point is situated near the surface as an approximation of the seismic source provoked by the Chelyabinsk bolide (54.5939° N, 63.4186° E), for a depth 100 m into the solid model. The event time is 03:20:36, which corresponds to the occurence time of an eventual impact, after the trajectory used in this work. The seismic moment is purely diagonal and each component is $1.0 \cdot 10^{16}$ N.m. The use of a larger moment for the source located on the ground is associated to the effect on the amplitude of waves generated by sources on the ground compared to those in the atmosphere. This effect is referred in section 1.5 and discussed in detail in section 2.2, for the comparison of the amplitudes generated by sources on the ground and located in the atmosphere. Waveforms of both data and synthetics are filtered between 10 and 50 seconds. 10 seconds is the minimum period sustained by the modeling with SPECFEM3D. The flat response of the instruments was chosen to be 50 seconds.

We show a comparison of the computed synthetics for the 1D model and the 3D model with recorded data for the 9 stations on Figure 15. The overall fit between data and synthetics is shown in Figure 15 where the data are shown in black, the synthetic

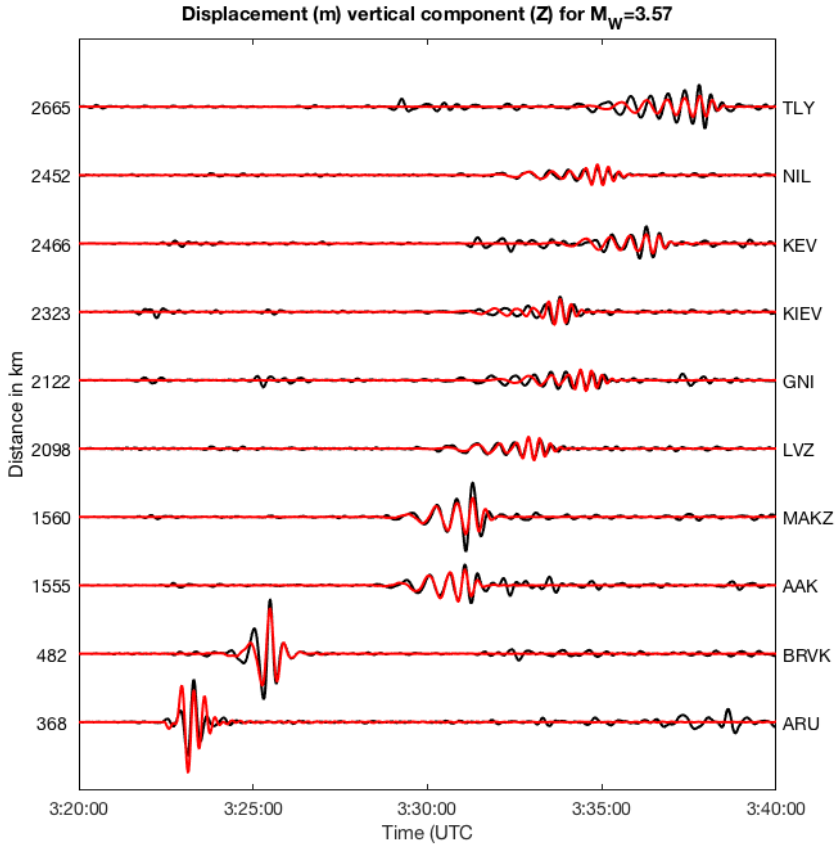

Fig. 14 The results of the inversion performed to the ensemble of the stations are shown in terms of synthetic seismograms for the vertical component of displacement, in red color. Black color represents the data for the vertical component of the displacement seismogram, for each one of the stations, indicated in the right axis. Data and synthetics are filtered between 0.015 Hz and 0.050 Hz.

seismograms calculated for the 1D model in red on the left part and those calculated for the 3D model in blue on the right part.

The fit for the whole period band is greatly better for the 3D model than for the 1D model. The cross-correlation coefficient computed between synthetics and recorded waveforms reaches values of 30% for the 1D model whereas this number clearly improves for the 3D model, ranging between 60% and 90%. We deduce that some of the variability of waveform observed in the data is explained by the 3D *3362iso* model complemented by *Eucrust 7.0*. The result is confirmed at the time delay between data and synthetics.

Another comparison between the results of these two modeling techniques was performed for the time delay of the synthetic seismograms, compared to the data.

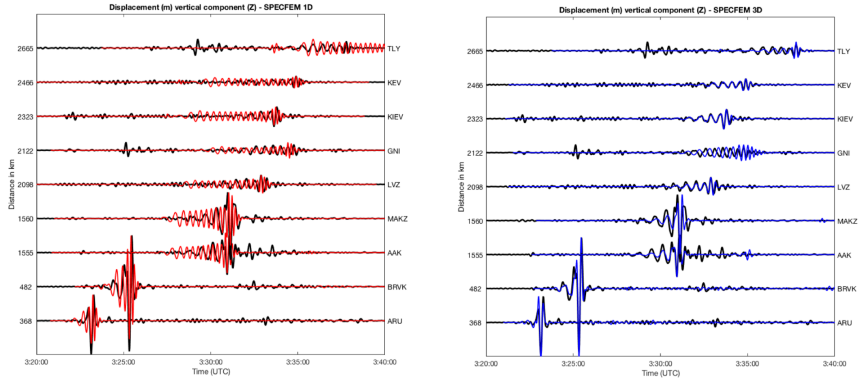

Fig. 15 Waveforms between 10 and 50s of the vertical component of displacement seismograms. Recorded data are in black, computed synthetics in color. The gray curves indicate arrival times with move-out speed between 4.5 and 2.3 $km.s^{-1}$, corresponding as a first approximation to the time-window of arrival of Rayleigh waves. On the left part, the synthetics computed with 1D model are shown in red, whereas the synthetics computed with the 3D model (crustal structure and attenuation included) are shown in blue on the right part.

Table 5 Time delay between the synthetic seismograms and data, for 9 stations and for each methodology used. * NMS = Normal modes summation. ** SEM = Spectral Element Method

Station	NMS 1D	SEM 1D	SEM 3D
ARU	21.2 s	168.2 s	237.3 s
BRVK	27.7 s	83.3 s	134.0 s
AAK	26.5 s	135.5 s	93.25 s
MAKZ	27.7 s	172.75 s	108.3 s
LVZ	29.8 s	78.10 s	13.45 s
GNI	108.7 s	165.25 s	45.60 s
KIEV	12.9 s	99.35 s	3.25 s
KEV	72.9 s	-56.5 s	13.85 s
TLY	60 s	224.5 s	161.70 s

In order to perform the inversion of the synthetic seismograms calculated with the normal modes summation we performed a time shift. This means that we minimized the time difference between the arrivals on the data-series and the computed ones on the synthetics. This time delay is shown in Table 5 and it is compared with the time shift for the synthetic seismograms calculated with spectral element method, for an 1D and 3D crustal model.

1.9 Discussion

With a source modeling based on the calculation of synthetic seismograms by normal modes summation (Lognonné et al., 1998) and the development of a purely linear physical approach, we are able to model the Rayleigh waves generated by a meteor which enters the Earth atmosphere. The results of our approach are in coherence,

with those provided in previous works, concerning the released energy (Brown et al., 2013) and the properties of the seismic event (Tauzin et al., 2013).

We performed a step forward in the source modeling, compared to previous works with an inversion of the moment tensor, by providing a line source located in the atmosphere, with an approach of consecutive explosions. We present a linear far field approach for the modeling of a source that generates nonlinear waves in the near field.

Compared to previous works that modeled a point source with normal modes summation (Heimann et al., 2013) for the same event, we provide a more complex and realistic location of the source and perform our investigation in a broader frequency domain. We perform the inversion of the vertical component of Rayleigh waves, in the displacement seismograms recorded by the stations of GSN for Chelyabinsk meteoroid, as Tauzin et al. (2013) and Heimann et al. (2013), and, in addition, we extend our investigation to the horizontal components and the velocity and acceleration seismograms in order to validate our results and look further into the seismic signature of such a source.

The ensemble of our findings, for inversions performed to all components of all seismograms of all the selected stations, appears to be in coherence, with the moment magnitude provided by all our experiments to be between $Mw = 3.54$ to 4.03 (Table 3), whereas the inversions applied to the ensemble of the stations provide results between $Mw = 3.45$ to 3.70 (Table 4). We do not make any assumption for the duration of every source, as this is contained in the final result of the provided moment.

Any deviation of the Rayleigh waveforms between the recordings and the synthetic seismograms, which is not important compared to their amplitude, can be expected when seismograms calculated for an 1D spherically symmetric model of the Earth are compared to real data. This is evidence that a method of source inversion of linear atmospheric sources based on the modeling of the Rayleigh waves by normal modes summation can be used as the basis for an inversion of the crustal structure, mainly in local scale but even in larger distances in the case of a great event. In order to test this assumption, we calculated the synthetic seismograms for Chelyabinsk meteoroid using a spectral element method software. The results of this test showed a better correlation of waveforms calculated for a 3D model including crustal structure and attenuation compared to the 1D one.

In addition, an eventual inversion based also in the contribution of the atmospheric waves, by the respective computation and summation of the acoustic normal modes, can contribute to our further understanding for the processes occurring in the atmosphere during airburst events. In order to perform this task, the availability of data from stations in short epicentral distances ($< 1^\circ$) is necessary.

2 Modeling of the Rayleigh waves generated by a meteor impact on Mars

Seismology is considered today one of the best tools to investigate planetary interiors. Meteoroid impacts constitute a very important seismic source, since their locations and, in some cases, their occurrence times can be accurately known from orbiters, tracking or optical observations. Their contribution is enhanced in the case of a seismic experiment SEIS (Seismic Experiment of Interior Structure) on board

the next Martian mission"InSight" (Interior Exploration using Seismic Investigations, Geodesy and Heat Transport) (Banerdt et al., 2013), as the known location allows a direct inversion of differential travel times and wave forms for structure identification. For InSight, the impact locations might be detected by the CTX camera (Malin et al., 2007) of the Mars Reconnaissance Orbiter.

In the first part of this work, we performed an inversion of a seismic source, corresponding to the entry of a meteor in the atmosphere of the Earth. As indicated in the latter section 1.9, the modeling of atmospheric sources with normal modes summation can be a useful tool for the investigation of the crustal, or even more, the lithospheric structure. The provided results for a known source on Earth, in coherence with the already known properties of the examined event, allow the application of the same method of modeling of seismic sources associated to meteor entries in planetary atmospheres, in another planet.

In this case, we perform a calculation of synthetic seismograms by normal modes summation on Mars, aiming to provide evidence about their detectability by the SEIS instrument and discuss the properties of the Rayleigh waves generated by them in the extraterrestrial environment, where InSight data are supposed to be the first seismic recordings.

2.1 Normal modes computation

We performed the computation of solid spheroidal normal modes for a whole planet (solid part and atmosphere). The solid part is the *AR model* of Mars interior (Okal and Anderson, 1978), an 1D model that we assume in spherical symmetry. An atmospheric model of Mars, *LMD* (Spiga et al., 2010), containing information about the viscosity of the Martian atmosphere and the relaxation of CO_2 into it, is adjusted on the model of the solid internal structure.

We computed the spheroidal solid modes for a whole planet by applying a radiant boundary on the top of the atmosphere, the relaxation of CO_2 into it, and the viscosity effects, for angular orders up to $l = 1200$ and frequencies up to 0.16 Hz. The calculated amplitudes for the vertical component of the fundamental mode in the atmospheric part of the provided model appear to be much larger than the same for the overtones, whereas the energy fraction in the atmosphere is about 10 times larger for the fundamental mode, compared to this for the overtones. This is a first indication that the fundamental mode should be dominant in any synthetic seismogram calculated for an atmospheric source.

This effect is shown in Figure 16 where the real part of the radial component of the fundamental solid spheroidal mode, in the atmosphere of Mars, is shown on the left, whereas the respective component of its first overtone is shown on the right. We note that the amplitudes provided for the fundamental mode are about 3.35 times greater than the respective for the overtone.

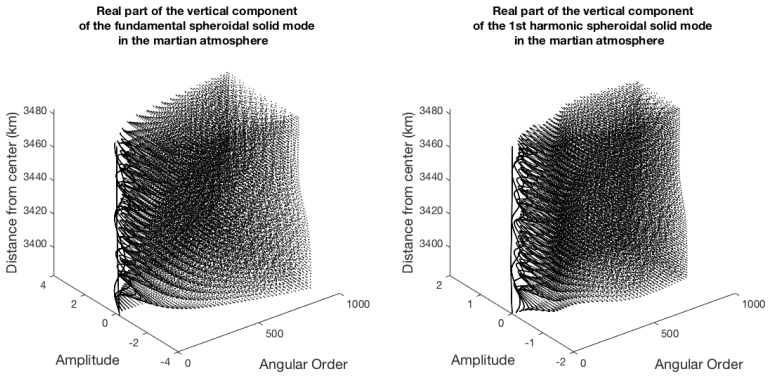

Fig. 16 The amplitudes of the vertical component of the real part of spheroidal solid modes in the atmosphere of Mars. On the left the amplitudes of the fundamental mode are shown, whereas on the right, those of the 1st overtone. A radiant boundary condition is applied on the top of the atmospheric model, whereas the relaxation of CO_2 and the viscosity in the Martian atmosphere are applied. The amplitudes corresponding to the fundamental mode appear to be two times larger than those of the 1st overtone.

2.2 Synthetic seismograms calculation

In order to examine the synthetic seismograms of an airburst in the Martian atmosphere and an impact, which occurs on Mars, we modeled two different events, with common characteristic the absolute value of the seismic moment. This value is estimated for a meteoroid impact corresponding to a 2-m diameter rocky impactor, as described in Section 2.2.1. Afterwards, the same absolute value of the seismic moment was used for an airburst at an altitude of 7 km, in order to compare the seismograms of equivalent sources, which, however, do not correspond to similar impactors.

2.2.1 Point source on the ground

We performed a first test of a source on the ground. The properties of the source are based on the theory of Holsapple (2003, 2007, 2015, 2017, 2018) and calculations were made in the provided platform.

As shown in Table 6 we consider a 2-m diameter rocky impactor moving at 10 $km.s^{-1}$ through the Martian atmosphere. The impactor's mass is calculated as a result of its density and size and the released energy is considered to be $6.28 \cdot 10^{11}$ J. Given the expression 4, the seismic moment in the triatomic Martian atmosphere should be $M_0 = 0.29 \cdot E$. Therefore we obtain a seismic moment equal to $M_0 = 1.8 \cdot 10^{11}$ N.m.

We used this isotropic point source, situated on the ground, for the calculation of synthetic seismograms at epicentral distances for every 5° (296.4 km on Mars), from 5° to 45°. The amplitudes of the Rayleigh modes summation, for frequencies up to 0.16 Hz, at an epicentral distance of 5° are shown in Figure 17. The presented synthetic seismogram is the pure summation of normal modes, without the application of any filter. Therefore, the frequency domain contains frequencies from 0.001 Hz to 0.16 Hz, the highest frequency of computed normal modes.

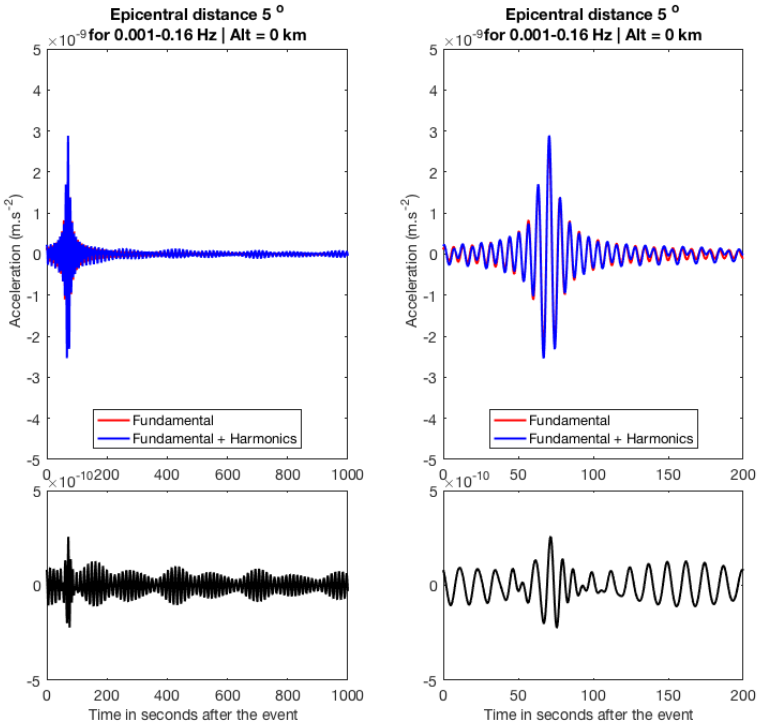

Fig. 17 The synthetic seismogram calculated for a source located on the ground, of $M_W = 1.36$, in a station located at an epicentral distance of 5°. The right part is a zoom in the waveform shown on the left part. The synthetic seismogram calculated by summation of the fundamental mode is shown in red, whereas the one calculated by summation of the fundamental mode and the first two harmonics is shown in blue. On the bottom part, the residual between the red and blue seismograms is presented. We can deduce that harmonics have a minor contribution to the calculated synthetic seismograms.

The seismogram calculated for the fundamental mode is shown in red, whereas the blue color indicates the seismogram calculated by the summation of the fundamental mode and its two overtones. In the bottom part the residual between these two seismograms is shown. We can notice that the contribution of the overtones is barely observed as it corresponds to amplitudes close to the noise level and therefore its contribution to the Rayleigh waveform is minor. Therefore, the fundamental mode dominates the seismogram, a condition that applies also to the case of Chelyabinsk meteoroid and is referred to in section 1.5.

This effect can be explained, as the fundamental mode describes better the displacement near the surface, whereas the overtones correspond to displacement in greater depths. The frequency domain of our investigation concerns the Rayleigh waves and therefore a more important contribution of the overtones is possible to be observed in higher frequencies.

2.2.2 Point source in the atmosphere

After the calculation of synthetic seismograms for a ground explosion, we investigated the waveforms provided by the same technique, for the Rayleigh waves generated by sources in the atmosphere. More precisely, we used a point source at a low altitude in the Martian atmosphere, for an equivalent value of the moment tensor.

It is important to note that equal moment tensor in different altitudes in the atmosphere indicates a meteoroid of different size. Therefore, in this case, the provided synthetic seismograms for a point source in the atmosphere concern another meteoroid, bigger than this examined in the previous section 2.2.1. The approach to model the explosions of the same meteoroid in different altitudes is used in the source inversion performed for Chelyabinsk and is described in detail in section 1.2.

Miljković et al. (2016) showed that a meteoroid of 2 m diameter, of either cometary or carbonaceous composition, traveling with the speed of 10 $km.s^{-1}$ in the Martian atmosphere, will first burst at an altitude of about 7 km. Therefore, we place the described source in this altitude, in order to perform the calculation of the synthetic seismograms in a similar way as it is done for the source on the ground.

The synthetic seismograms for this source are shown in Figure 18. The right part of the Figure is a zoom in the Rayleigh waveform of the data series on the left part. We observe that the amplitude of Rayleigh waves for a source of $M_W = 1.36$, is larger than the one obtained for a source on the ground (Figure 17), whereas the arrival time is earlier. The residual between the summation of the fundamental mode and the seismogram with the addition of its two first overtones indicates that for atmospheric sources the harmonics have an, equal to the impact case, minor contribution to the amplitudes of the Rayleigh waves, generated by the coupling between the solid and atmospheric part of the planet.

2.3 Detectability of the meteor impact events

As referred in the introduction of this section 2, part of our aim to perform the modeling of Rayleigh waves generated by meteoroid impacts on Mars is to provide evidence for their detectability by the SEIS VBB seismometer of InSight mission. In our modeling of the source on the ground and the Martian atmosphere, we assume a 2-m impactor. However, in the period of 2 terrestrial years, while the operations of InSight on Mars will take place, impacts of such size are considered to be very rare.

Although the model by Miljković et al. (2016) is simplified, and in reality it does not mean that only one airburst would occur during the atmospheric passage, here we also consider smaller impactors, that are also more frequent and more likely to occur during the lifetime of the InSight mission. It is also convenient that even a simplified model by Miljković et al. (2016) indicates that smaller size impactors are more probable to hit the Martian ground without any mass loss, if other conditions, as their speed, permit so. Similarly to the 2-m impactor, we calculate the scaling relationship (Holsapple (2003, 2007, 2015, 2017, 2018)) for 1-m and 0.5-m impactors (6). In these calculations we consider a target consisted of regolith with a mass density $\rho = 1500\ kg \cdot m^{-3}$. In this study, this scaling applies to a small range of impactor

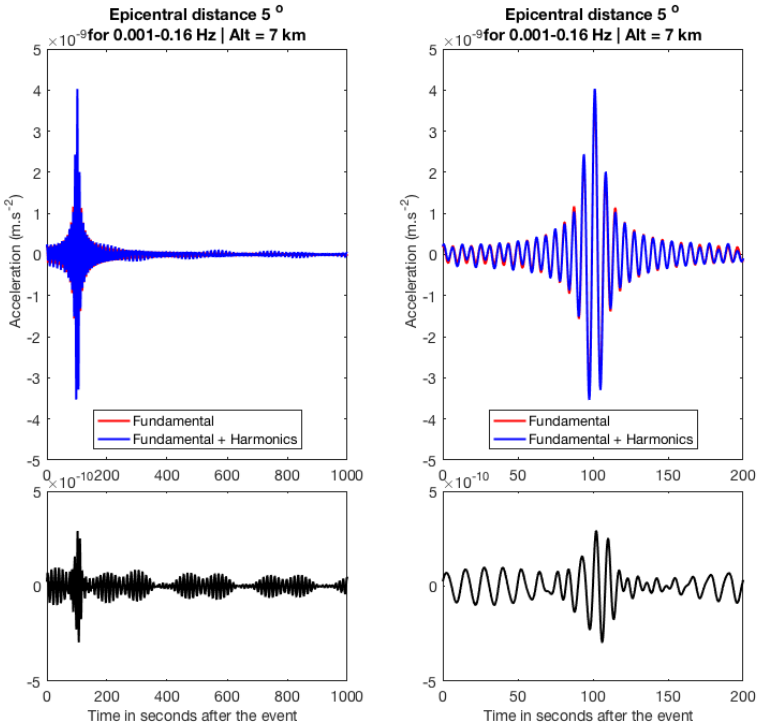

Fig. 18 The synthetic seismogram calculated for a point source in an altitude of 7 km in the Martian atmosphere, of $M_W = 1.36$, in a station located at an epicentral distance of 5°. The right part is a zoom in the waveform shown on the left part. The synthetic seismogram calculated by summation of the fundamental mode is shown in red, whereas the one calculated by summation of the fundamental mode and the first two harmonics is shown in blue. As observed also in Figure 17 the overtones appear to have a minor contribution to the Rayleigh waveform.

sizes. For all of them we consider an associated boxcar source time function, with a duration of $\tau = 1$ *sec*. Larger impacts may provide larger source durations, however this investigation is not the objective of the present work.

We also compute the released energy for these impacts hitting the ground. We are able to deduce the seismic moment of these impacts resulting to ground explosions by using the equation 4. The ratio of the seismic moment in each case, in comparison with the seismic moment of the impactor of a diameter of 2 meters, shown in the last row of Table 6, is going to be used in order to perform a scaling to the amplitudes calculated in sections 2.2.1 and 2.2.2. In order to obtain these values, we consider a rocky impactor, with a density of $\rho_{impactor} = 3300\ kg \cdot m^{-3}$, hitting vertically, with a velocity of $\upsilon = 10\ m \cdot s^{-1}$ a surface of regolith, characterized by a density of $\rho_{target} = 1500\ kg \cdot m^{-3}$, a friction angle $\phi = 40^{\circ}$ and porosity $\nu = 0.4$ whereas the Martian gravity is $g = 3.71\ m \cdot s^{-1}$.

Table 6 Scaling of the seismic moment (in $N \cdot m$) for different sizes of meteoroids reaching Martian ground, based on Holsapple (2003, 2007, 2015, 2017, 2018). The model considers the velocity of the impactor $\upsilon = 10\ km \cdot s^{-1}$ and its density $\rho = 3000\ kg \cdot m^{-3}$. The target is a regolith surface, with a density of $\rho_{target} = 1500\ kg \cdot m^{-3}$, a friction angle $\phi = 40°$ and porosity $\nu = 0.4$. The Martian gravity is $g = 3.71\ m \cdot s^{-2}$.

Impactor Diameter (m)	2	1	0.5
Crater Diameter (m)	33.74	17.78	9.20
Crater Depth (m)	9.20	4.85	2.51
Mass (kg)	12600	1570	196
Energy (J, T eq. TNT)	$6.28 \cdot 10^{11}$ (150)	$7.85 \cdot 10^{10}$ (18.76)	$9.82 \cdot 10^{9}$ (2.35)
Moment (N.m)	$1.8 \cdot 10^{11}$ ($M_W = 1.36$)	$2.24 \cdot 10^{10}$ ($M_W = 0.76$)	$2.8 \cdot 10^{9}$ ($M_W = 0.16$)
Scaling	1	0.124	0.016

In Figure 19, the spectra of the seismograms presented in sections 2.2.1 and 2.2.2 are presented in black color. The red continuous line and the blue line represent the spectra for smaller impacts (1 m and 0.5 on the ground respectively) obtained by the scaling of the seismic moment. The dashed red line indicates the SEIS VBB requirement of the InSight mission. We can deduce that only a fraction of the provided amplitudes of Rayleigh waves is supposed to be detected in this frequency domain, even in small epicentral distances (5°). More precisely, the impacts of diameter equal to 0.5 meter, that explode on the Martian ground, will be detectable only in higher frequencies of the Rayleigh waves. Therefore, we deduce that the investigation of this kind of events, should be focused on the highest frequencies of Rayleigh waves, in the order of 0.2 Hz, in order to detect their seismic signature.

In order to estimate the maximum epicentral distance of detectability of a 1-meter diameter meteoroid, we use the following equation 11 which describes the attenuation of the Rayleigh waves:

$$S(\Delta) = S(5°) \cdot \sqrt{\frac{sin\,(5°)}{sin\,(\Delta)}} \cdot exp\left(-\frac{\omega\, t_R}{2Q}\right) \tag{11}$$

where $S(5°)$ is the amplitude density of the signal at an epicentral distance of 5° (the distance of the spectra presented in Figure 19), Δ the epicentral distance along the same azimuth, ω the angular frequency, given by $\omega = 2\pi f$ and in this case $f = 0.16$ Hz, t_R the propagation time of the waves, given by $t_R = \frac{\Delta}{\upsilon_g}$ with υ_g to be the velocity of Rayleigh waves, considering that in these frequencies there are no dispersion effects and finally Q is the anelastic attenuation factor.

In Figure 20 the results of these calculations are shown for $Q = 250,\ 500,\ 1000$, in black, blue and red color respectively. The noise level during a Martian day is indicated by the red dotted line. In order to record the signal of a meteor impact, it should be greater than $10^{-9}\ m.s^{-2}.Hz^{-1/2}$. Therefore, we calculate the epicentral distances where such an amplitude can be recorded. In the mean time, we perform the same calculation for a more satisfactory signal, greater than $2 \cdot 10^{-9}\ m.s^{-2}.Hz^{-1/2}$. The results for the maxima distances where these signals can be recorded are shown in Table 7.

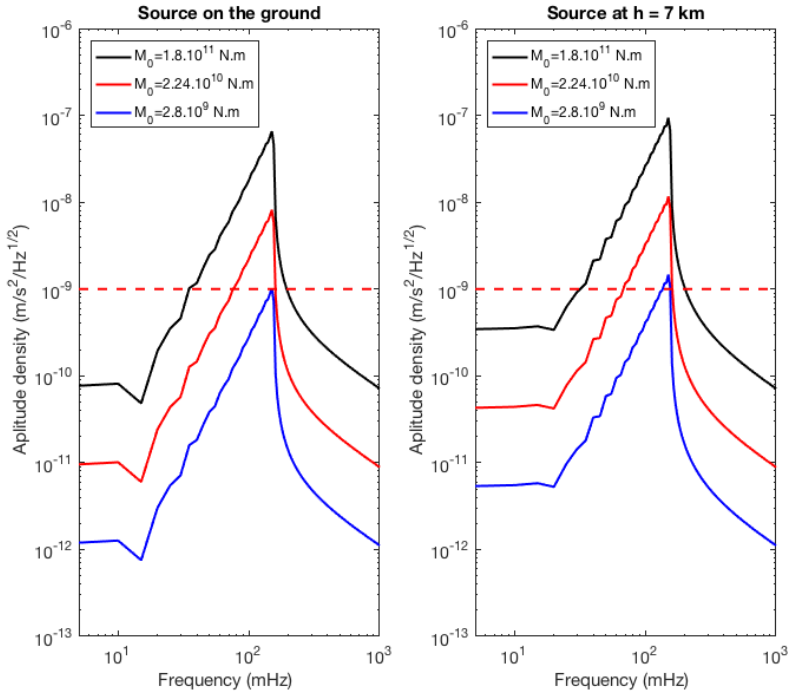

Fig. 19 The spectra of the seismograms calculated for point sources situated on the ground (on the left) and in an altitude of 7 km (on the right), for a station located in an epicentral distance of 5°. The black line shows the spectra of the seismograms for a seismic moment $M_0 = 1.8 \cdot 10^{11}\ N \cdot m$, corresponding to an meteor impact for a meteoroid of a diameter of 2 m on the ground, whereas the continuous red line and the blue line show the amplitude density of synthetic seismograms obtained by scaling and corresponding to ground explosions of impactors of a diameter of 1 and 0.5 m respectively. We should underline that these spectra do not concern the same impactor. In order to obtain the same moment from an explosion on the ground and at an altitude in the atmosphere of a planet, the impactor exploded in the atmosphere should be much larger than the one which hits the ground.

Table 7 Maxima distances where the signal of an 1 meter diameter impact can be recorded by SEIS VBB seismometer, of InSight mission on Mars.

Q	$max(\Delta)$ for $S(\Delta) \geq 10^{-9}\ m.^{-2}.Hz^{-1/2}$	$max(\Delta)$ for $S(\Delta) \geq 2 \cdot 10^{-9}\ m.^{-2}.Hz^{-1/2}$
250	33.5° (1986.2 km)	21.5° (1274.7 km)
500	57° (3379.5 km)	33.5° (1986.2 km)
1000	109° (6462.5 km)	50.5° (2994.1 km)

2.4 Estimation of the number of detectable impacts during 1 Martian year

The number of detectable impacts, for crater diameters varying between 1 to 100 meters is summarized using various models by Daubar et al. (2018). In Table 6 we show that the crater diameter for an impactor of 1 meter diameter on Mars should

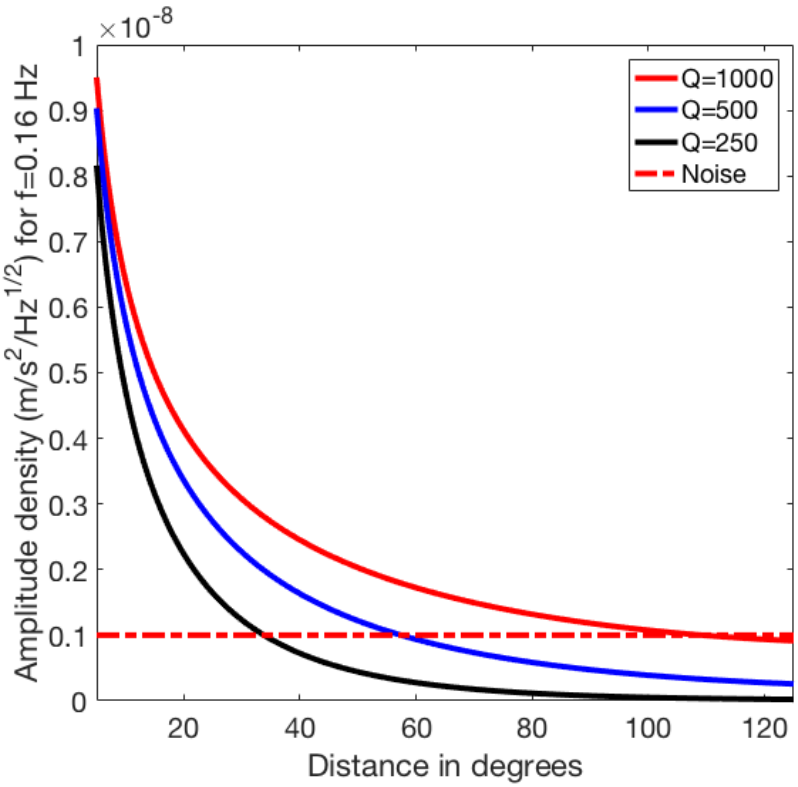

Fig. 20 The estimation of the amplitude density of the Rayleigh waves generated by an impact of 1 meter diameter, in epicentral distances from 5° is shown in black for $Q = 250$, blue for $Q = 500$ and red color for $Q = 1000$. The red dotted line indicates the noise level during a day on Mars, equal to $10^{-9}\ m.s^{-2}.Hz^{-1/2}$.

be 17.7 meters. According to Daubar et al. (2018), the minimum number of events which generate craters of this size or larger during one Earth year is $n = 15.7$ using the current impact rate measure by Daubar et al. (2013), whereas the most optimistic estimation is for $n = 31.4$.

In order to estimate the number of detectable events we calculate the number of impacts which should occur in an area corresponding to the epicentral distances indicated in Table 7. The curves represent the estimations for $Q = 250$ in black, $Q = 500$ in blue and $Q = 1000$ in red color respectively. The dashed lines correspond to the estimations for the lower rate of impacts (Daubar et al., 2018) whereas the continuous lines to the higher one. The number of detectable events is corresponding to those characterized by an amplitude density greater than $10^{-9}\ m.^{-2}.Hz^{-1/2}$ for high frequency Rayleigh waves, $f = 0.16Hz$.

The numerical values of these results are also presented in Table 8 where the estimated number of the detectable impacts of a diameter of 1 meter, for $Q = 250,\ 500,\ 1000$, for one Earth year and one Mars year (period of InSight operations) according to the lower and higher impact rate estimated by Daubar et al. (2018), is shown. The cal-

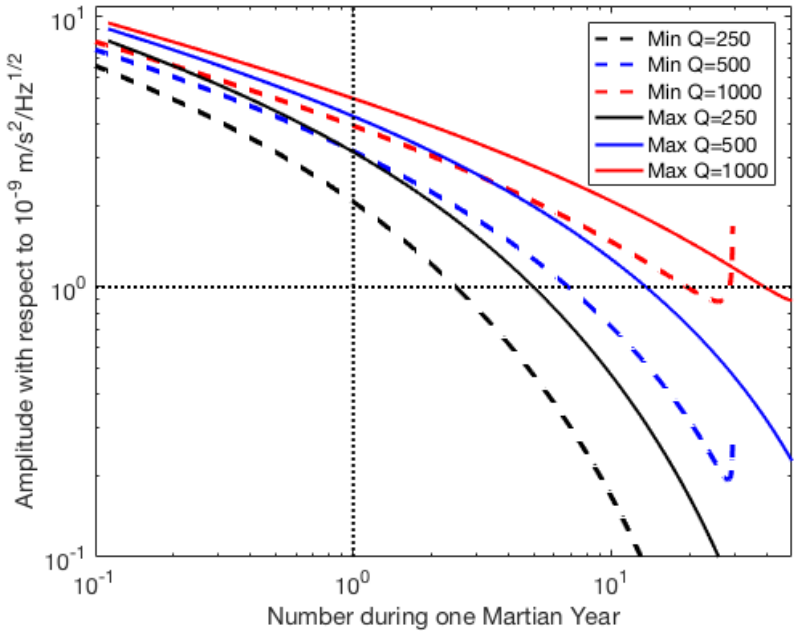

Fig. 21 The estimation of the number of detectable impacts during 1 Martian year (period of InSight operations on Mars = 1.8808 years on Earth). The curves corresponding to $Q = 250$ are shown in black, $Q = 500$ in blue and $Q = 1000$ in red. The dashed lines correspond to a lower impact rate, whereas the continuous ones to a higher one.

Table 8 The number of detectable meteor impacts of d = 1 meter for one Earth year and one Mars year, for $Q = 250,\ 500,\ 1000$, based on the impact rate estimations by Daubar et al. (2018).

	1 Earth year		1 Mars year	
Q	Lower impact rate	Higher impact rate	Lower impact rate	Higher impact rate
250	1.3031	2.6062	2.4509	4.9017
500	3.5749	7.1498	6.7237	13.4473
1000	10.4060	20.8120	19.5716	39.1432

culations concern the detectability during daytime and the estimated numbers can be twice greater for night conditions, where the amplitude of the noise is much smaller.

These estimations appear to be less optimistic than those presented by Teanby (2015), where there are predicted 0.1 to 30 impacts per Earth year, for craters in the 2 to 40 meters diameter range, with a minimum amplitude density of $10^{-8}\ m.^{-2}.Hz^{-1/2}$.

Compared to the estimations for the number of detectable impacts by Daubar et al. (2018), based on the propagation of body waves in the solid part of the planet, in the present work the atmospheric part is integrated and the estimations are based on the propagation of surface waves.

As it concerns the airbursts, our estimated number of detectable events, even in short epicentral distances is much smaller than the one estimated by Stevanović et al.

(2017), who predict $\sim 20-100$ detectable airbursts by InSight seismometer. Our analysis for a similar moment tensor in the altitude of 7 km in the Martian atmosphere, shows that the obtained signal should be higher by an order of $\sim 10\%$ (see Figure 19). However, the number of events able to provide this signal is much less. Following the physical approach performed for Chelyabinsk and presented in section 1.2 we can deduce that a larger meteoroid is needed in order to generate an explosion of $M_0 = 2.24 \cdot 10^{10}$ in this altitude.

3 Conclusion

We perform a comparative analysis of meteoroid impact events on the Earth and Mars with the source inversion of an airburst on Earth (Chelyabinsk) and the modeling of Rayleigh waves generated by ground and atmospheric explosions on Mars. The calculation of Rayleigh waves is done by normal modes summation (Lognonné et al., 1998).

In past works, the moment tensor inversion was performed for Chelyabinsk meteoroid, for point sources on the ground Tauzin et al. (2013) or in the atmosphere (Heimann et al., 2013). In this work we develop an approach for a line atmospheric source, constituted by consecutive explosions (point sources) in the atmosphere. This approach obeys to limitations in terms of temporal resolution, in order to avoid the linear summation of nonlinear effects associated to the supersonic speeds of a meteor entry in the atmosphere. The reconstruction of the source is based in the published properties of its trajectory (Borovička et al., 2013). Every explosion in the atmosphere is considered an isotropic moment tensor, nevertheless, the radial component dominates the provided seismograms, as the contribution of both the other diagonal components of the moment tensor appears to be smaller than 1% to the provided waveforms.

We calculate synthetic seismograms in a broad band of Rayleigh wave frequencies, from 0.015 Hz up to 0.050 Hz, for a set of 10 stations, which were selected after research for the best quality of available data, in terms of Rayleigh waveforms.

In order to find the source which satisfies the best fit between the synthetic seismograms and the recordings, we use an inversion technique based on the singular value decomposition (Rakoto et al., 2018). The inversion technique is applied separately in every seismogram for the horizontal and vertical components of displacement, velocity and acceleration, provided for every station, and in a second step to artificial time series consisting a composition of the Rayleigh waveforms modeled or recorded for the whole set of selected stations.

The moment magnitude obtained by the inversion of Chelyabinsk Rayleigh waves varies between $M_W = 3.45$ to $M_W = 3.70$, which is in agreement with previous works computing the total amount of the released energy (Brown et al., 2013).

Thereafter, we apply the same modeling technique of normal modes summation in order to obtain Rayleigh waveforms for meteor impacts occurring on the Martian ground or the lower altitudes of the atmosphere. We observe the dominance of the fundamental solid mode on the provided waveforms, compared with the contribution of its two overtones. By performing a scaling on the spectra of the Rayleigh am-

plitudes we deduce that small impactors, in the diameter range of 0.5 to 2 m, can be detectable in short epicentral distances only in the high frequency domain of Rayleigh waves (up to 0.2 Hz).

Finally we perform an analysis based on the impact rate estimated by Daubar et al. (2018) in order to provide an estimation for the number of detectable impacts, for craters 17.78 meters of diameter (corresponding to meteoroids of 1 meter diameter). We find the epicentral distances up to which these events can be detected by the SEIS VBB seismometer of InSight mission. Thereafter, we calculate the number of events expected to be detected in a period of 1 Martian year, for $Q = 250,\ 500,\ 1000$. During one Mars year of InSight operations, we expect 6.7 to 13.4 detectable impacts ($Q = 500$).

This work of comparative analysis of Rayleigh waves on Earth and Mars provides evidence that seismic modeling by normal modes summation, on the basis of a known 1D model for the solid part and the atmosphere, in spherical symmetry, can be a useful tool for planetary seismology. On Earth, our methodology is found efficient to identify the characteristics of a seismic source and provide satisfactory results for complex sources in high frequencies of the Rayleigh waves (up to 0.05 Hz). This knowledge can be used in order to model similar events in different atmospheric conditions and deduce the properties of the crustal structure of a planet, mostly in local scale and rarer in larger regions, depending to the size of the impact.

Acknowledgements The facilities of IRIS Data Services, and specifically the IRIS Data Management Center, were used for access to waveforms, related metadata, and/or derived products used in this study. IRIS Data Services are funded through the Seismological Facilities for the Advancement of Geoscience and EarthScope (SAGE) Proposal of the National Science Foundation under Cooperative Agreement EAR-1261681. Spectral Element Modeling was performed on the HPC resources of LANL. A portion of this research was carried out at the Jet Propulsion Laboratory, California Institute of Technology, under a contract with the National Aeronautics and Space Administration. FK acknowledges the financial support of the UnivEarthS Labex program at Université Sorbonne Paris Cité (ANR-10-LABX-0023andANR-11- IDEX-0005-02) and of the SODERN company for his Ph.D. financial support. KM research is fully supported by the Australian Government (project numbers DE180100584 and DP180100661). We thank Raphaël Garcia and two anonymous reviewers for their constructive reviews. This is IPGP contribution xxxx. This is InSight contribution Number 73.

References

Banerdt W, Smrekar S, Lognonné P, Spohn T, Asmar SW, Banfield D, Boschi L, Christensen U, Dehant V, Folkner W, Giardini D, Goetze W, Golombek M, Grott M, Hudson T, Johnson C, Kargl G, Kobayashi N, Maki J, Hurst K, the InSight Team (2013) Insight: A discovery mission to explore the interior of mars. Lunar Planet Sci Conf 44:1915

Bassin C, Laske G, Masters G (2000) The current limits of resolution for surface wave tomography in north america. eos trans agu 81:f897. Eos Transactions American Geophysical Union 81:F897

Ben-Menahem A (1975) Source parameters of the Siberian explosion of June 30, 1908, from analysis and synthesis of seismic signals at four stations. Physics of the Earth and Planetary Interiors 11:1–35

Borovička J, Spurný P, Brown P, Wiegert P, Kalenda P, Clark D, Shrbený L (2013) The trajectory, structure and origin of the Chelyabinsk asteroidal impactor. Nature 503:235–237, DOI 10.1038/nature12671

Brown P, Assink J, Astiz L, Blaauw R, Boslough M, Borovička J, Brachet N, Brown D, Campbell-Brown M, Ceranna L, Cooke W, De Groot-Hedlin C, P Drob D, Edwards W, Evers L, Garces M, Gill J, Hedlin M, Kingery A, Krzeminski Z (2013) A 500-kiloton airburst over chelyabinsk and an enhanced hazard from small impactors. Nature 503:238–241, DOI 10.1038/nature12741

Daubar I, McEwen A, Byrne S, Kennedy M, Ivanov B (2013) The current martian cratering rate. Icarus 225(1):506–516, DOI 10.1016/j.icarus.2013.04.009

Daubar I, Philippe L, Teanby NA, Miljković K, Stefanovic J, Vaubaillon J, Kenda B, Kawamura T, Clinton J, Lucas A, Drilleau M, Yana C, Collins GS, Banfield D, Golombek M, Kedar S, Schmerr N, Garcia R, Rodriguez S, Gudkova T, May S, Banks M, Maki J, Sansom E, Karakostas F, Panning M, Fuji N, Wookey J, van Driel M, Lemmon M, Ansan V, Böse M, Stähler S, Kanamori H, Richardson J, Smrekar S, Banerdt WB (2018) Impact-seismic investigations of the insight mission. Space Science Reviews Same Issue

Dziewonski A, Anderson D (1981) Preliminary reference earth model. Physics of the Earth and Planetary Interiors 25:297–356, DOI 10.1016/0031-9201(81)90046-7

Edwards WN (2009) Meteor generated infrasound: Theory and observation. In: Le Pichon A, Blanc E, Hauchecorne A (eds) Infrasound Monitoring for Atmospheric Studies, Springer Netherlands, pp 361 – 414, DOI 10.1007/978-1-4020-9508-5-12

de Groot-Hedlin C, Hedlin MA (2014) Infrasound detection of the chelyabinsk meteor at the usarray. Earth and Planetary Science Letters 402:337 – 345, DOI https://doi.org/10.1016/j.epsl.2014.01.031, special issue on USArray science

Hanks TC, Kanamori H (1979) A moment magnitude scale. Journal of Geophysical Research: Solid Earth 84(B5):2348–2350, DOI 10.1029/JB084iB05p02348, URL https://agupubs.onlinelibrary.wiley.com/doi/abs/10.1029/JB084iB05p02348

Heimann S, González A, Wang R, Cesca S, Dahm T (2013) Seismic characterization of the chelyabinsk meteors terminal explosion. Seismological Research Letters 84(6):1021, DOI 10.1785/0220130042

Holsapple KA (2003, 2007, 2015, 2017, 2018) Users Manual: Crater Sizes from Explosions or Impacts by Keith A. Holsapple. http://keith.aa.washington.edu/craterdata/scaling/index.htm, accessed: 2018-02-16

International Seismological Centre (2013) On-line Bulletin. Internatl. Seismol. Cent., Thatcham, United Kingdom, http://www.isc.ac.uk

Komatitsch D, Tromp J (2002a) Spectral-element simulations of global seismic wave propagation-i. validation. Geophysical Journal International 149(2):390–412, DOI http://doi.org/10.1046/j.1365-246X.2002.01653.x

Komatitsch D, Tromp J (2002b) Spectral-element simulations of global seismic wave propagation–ii. three-dimensional models, oceans, rotation and self-gravitation. Geophysical Journal International 150(1):303–318

Le Pichon A, Ceranna L, Pilger C, Mialle P, Brown D, Herry P, Brachet N (2013) The 2013 russian fireball largest ever detected by ctbto infrasound sensors. Geophysical Research Letters 40(14):3732–3737, DOI 10.1002/grl.50619

Lognonné P, Mosser B, Dahlen FA (1994) Excitation of Jovian Seismic Waves by the Shoemaker-Levy 9 Cometary Impact. Icarus 11:180–195

Lognonné P, Clévédé E, Kanamori H (1998) Computation of seismograms and atmospheric oscillations by normal-mode summation for a spherical earth model with realistic atmosphere. Geophys J Int 135(2):388–406, DOI 10.1046/j.1365-246X.1998.00665.x, URL http://dx.doi.org/10.1046/j.1365-246X.1998.00665.x

Malin MC, Bell JF, Cantor BA, Caplinger MA, Calvin WM, Clancy RT, Edgett KS, Edwards L, Haberle RM, James PB, Lee SW, Ravine MA, Thomas PC, Wolff MJ (2007) Context camera investigation on board the mars reconnaissance orbiter. Journal of Geophysical Research: Planets 112(E5), DOI 10.1029/2006JE002808, URL https://agupubs.onlinelibrary.wiley.com/doi/abs/10.1029/2006JE002808, https://agupubs.onlinelibrary.wiley.com/doi/pdf/10.1029/2006JE002808

Miljković K, Sansom EK, Daubar IJ, Karakostas F, Lognonné P (2016) Fate of Meteoroid Impacts on Mars Detectable by the InSight Mission. In: Lunar and Planetary Science Conference, Lunar and Planetary Inst. Technical Report, vol 47, p 1768

Myers S, Begnaud M, Ballard S, Pasyanos M, Phillips W, Ramirez A, Antolik M, Hutchenson K, Wagner G, Dwyer J, Rowe C, Russell D (2010) A crust and upper mantle model of Eurasia and North Africa for Pn travel time calculation. Bull Seism Soc Am 100:640–646

Okal EA, Anderson DL (1978) Theoretical models for mars and their seismic properties. Icarus 33(3):514 – 528, DOI https://doi.org/10.1016/0019-1035(78)90187-2, URL http://www.sciencedirect.com/science/article/pii/0019103578901872

Picone JM, Hedin AE, Drob DP, C AA (2002) Nrlmsise00 empirical model of the atmosphere: Statistical comparisons and scientific issues. Journal of Geophysical Research: Space Physics 107(A12):SIA 15–1–SIA 15–16, DOI 10.1029/2002JA009430, URL https://agupubs.onlinelibrary.wiley.com/doi/abs/10.1029/2002JA009430

Rakoto V, Lognonné P, Rolland L, Coïsson P (2018) Tsunami wave height estimation from gpsderived ionospheric data. Journal of Geophysical Research: Space Physics 0(0), DOI 10.1002/2017JA024654, URL https://agupubs.onlinelibrary.wiley.com/doi/abs/10.1002/2017JA024654

ReVelle DO (1974) Acoustics of meteors effects of the atmospheric temperature and wind structure on the sounds produced by meteors. PhD thesis, University of Michigan, Ann Arbor, MI

Shuvalov V, Svetsov V, Popova O, Glazachev D (2017) Numerical model of the chelyabinsk meteoroid as a strengthless object. Planetary and Space Science 147:38 – 47, DOI https://doi.org/10.1016/ j.pss.2017.05.011, URL http://www.sciencedirect.com/science/article/pii/S0032063316302781

Spiga A, Forget F, Lewis S, DP H (2010) Structure and dynamics of the convective boundary layer on mars as inferred from large-eddy simulations and remote-sensing measurements. Q J R Meteorol Soc 136:414–428, DOI 10.1002/qj.563

Stevanović J, Teanby NA, Wookey J, Selby N, Daubar IJ, Vaubaillon J, Garcia R (2017) Bolide airbursts as a seismic source for the 2018 mars insight mission. Space Science Reviews 211(1):525–545, DOI 10.1007/s11214-016-0327-3, URL https://doi.org/10.1007/s11214-016-0327-3

Tauzin B, Debayle E, Quantin C, Coltic N (2013) Seismoacoustic coupling induced by the breakup of the 15 february 2013 Chelyabinsk meteor. Geophysical Research Letters 40:1–5, DOI 10.1002/grl.50683

Teanby N (2015) Predicted detection rates of regional-scale meteorite impacts on mars with the insight short-period seismometer. Icarus 256:49 – 62, DOI https://doi.org/10.1016/j.icarus.2015.04.012, URL http://www.sciencedirect.com/science/article/pii/S0019103515001475

Tesauro M, Kaban MK, Cloetingh SAPL (2008) Eucrust07: A new reference model for the european crust. Geophysical Research Letters 35(5), DOI 10.1029/2007GL032244, URL https://agupubs.onlinelibrary.wiley.com/doi/abs/10.1029/2007GL032244

Zuluaga J, Ferrin I, Geens S (2013) The orbit of the chelyabinsk event impactor as reconstructed from amateur and public footage. arXiv:13031796